

**SINGLE-PIXEL CAMERA BASED SPATIAL
FREQUENCY DOMAIN IMAGING FOR
NON-CONTACT TISSUE CHARACTERIZATION**

A thesis submitted in partial fulfillment
of the requirements for the degree of
Master of Science in Biomedical Engineering

by

Alec M. Petrack
B.S.B.E., Wright State University, 2018

2020
Wright State University

Wright State University
GRADUATE SCHOOL

July 8, 2020

I HEREBY RECOMMEND THAT THE THESIS PREPARED UNDER MY SUPERVISION BY Alec M. Petrack ENTITLED Single-Pixel Camera Based Spatial Frequency Domain Imaging for Non-Contact Tissue Characterization BE ACCEPTED IN PARTIAL FULFILLMENT OF THE REQUIREMENTS FOR THE DEGREE OF Master of Science in Biomedical Engineering.

Ulas Sunar, Ph.D.
Thesis Director

John C. Gallagher, Ph.D.
Chair, Department of Biomedical & Human Factors Engineering

Committee on
Final Examination

Josh Ash, Ph.D.

Tarun Goswami, D.Sc.

Ulas Sunar, Ph.D.

Barry Milligan, Ph.D.
Interim Dean of the Graduate School

ABSTRACT

Petrack, Alec M. M.S.B.M.E., Department of Biomedical, Industrial and Human Factors Engineering, Wright State University, 2020. *Single-Pixel Camera Based Spatial Frequency Domain Imaging for Non-Contact Tissue Characterization*

Optical imaging has demonstrated potential as a medical imaging modality for measuring tissue functionality. Recently, interest in fluorescence guided surgery has emerged from improvements in optical imaging that have allowed real-time feedback. Of the optical imaging modalities, spatial frequency domain imaging (SFDI) has gained a lot of interest. Unlike spectroscopic techniques, such as functional near infrared spectroscopy (fNIRS) and frequency domain spectroscopy that measure bulk tissue properties, SFDI quantifies tissue functionality locally and wide field making it practical for clinical applications. Unfortunately, traditional SFDI systems use multi-pixel detectors, which may not exhibit ideal spectral characteristics, have limited sensitivity, be expensive, or bulky in size. On the other hand, avalanche photodiodes (APD) and single photon counting modules (SPCM), are much more sensitive to the spectrum ideal for optical imaging, inexpensive, and compact in size. Traditionally, an array of photodiodes are required to capture an image, but with the advent of single pixel cameras entire images can be captured with a single photodiode.

In this thesis, a novel single pixel camera (SPC) is used to capture an image of the light field projected by an SFDI system to explore its feasibility as a detection method relative to a traditional charged-coupled device (CCD) or scientific complementary metal-oxide semiconductor (sCMOS) camera. To determine the feasibility of single pixel SFDI, both sCMOS and SPC SFDI implementations were built to measure the optical properties of a brain tissue simulating phantom. In the results chapter, the mean optical scattering and absorption properties are reported for regions of high and low optical absorption indicating single pixel camera spatial frequency domain imaging (SPC SFDI) is viable given certain applications.

In Chapter 1, I provide the motivation and significance of single pixel spatial frequency domain imaging (spSFDI) in a clinical setting of neurological disease. Chapter 2 consists of theory and methods behind spSFDI. Chapter 3 covers the instrumentation setup and results from our tissue simulating phantom experiments. Finally, Chapter 4 concludes with final thoughts on the application space of spSFDI and methods to improve its implementation. From our phantom experiment results, spSFDI demonstrates it can obtain optical properties within 10 percent error, which is comparable to traditional SFDI instrumentation. This method is expected improve optical parameter quantification and have further applications in fNIRS research field related to diagnosis and therapy monitoring.

Contents

1	Introduction	1
1.1	The Need for Imaging Contrasts for Clinical and Preclinical Research	1
1.2	Optical Absorption and Scattering Contrasts in Diffuse Optical Imaging for Brain Tissue Characterization	2
1.3	The Proposed Approach: Single-Pixel Spatial Frequency Domain Imaging for Non-contact, Wide-Field Optical Imaging	5
2	Theory	8
2.1	Photon Diffusion in the Spatial Frequency Domain	8
2.1.1	Projection and Demodulation of Spatially Varying Modulated Light	10
2.1.2	Normalized Reflectance and Optical Property Quantification	11
2.2	Compressed Single Pixel Imaging	16
2.2.1	Image Compression	17
2.2.2	Compressive Sampling	19
2.2.3	Acquiring Compressed Samples in the Optical Domain	24
2.2.4	Sparse Signal Recovery	27
2.2.5	Compressed Single Pixel Spatial Frequency Domain Imaging	33
3	Experiment Methods and Validation	36
3.1	Single Pixel Spatial Frequency Domain Imaging Instrument	36
3.1.1	spSFDI Instrument Response Characterization with Brain Tissue Mimicking Phantoms	41
4	Conclusions and Future Works	46
4.1	Real-Time Single Pixel Imaging	46
4.2	Real-Time SFDI Optical Property Map Extraction with Deep Learning	47
4.3	Improving Signal to Noise Ratio of Single Pixel Camera	49
Bibliography		50

List of Figures

1.1	Photons highly scatter or get absorbed in living tissue like brain before reaching to photon detector.	3
1.2	Molar extinction (absorption) coefficient of oxygenated and deoxygenated hemoglobin with respect to wavelength in brain tissue. The isosbestic point is the wavelength, which oxygenated and deoxygenated hemoglobin attenuate light equally.	4
1.3	Optical scattering and absorption parameters provide contrast for Alzheimer's disease [18].	5
1.4	Noncontact spatial frequency domain imaging (SFDI) provides optical absorption and scattering contrasts in Alzheimer's disease [10].	7
2.1	SFDI projections captured from SFDI instrument. For a single spatial frequency, f_x , there are three phases.	11
2.2	Diffuse reflectance with respect to optical absorption and reduced scattering.	12
2.3	Flow chart for quantifying optical properties. In this example, there are two spatial frequencies that are demodulated and fit to obtain the optical property maps. Data provided from Open-SFDI.	13
2.4	Diagram of spatial frequency domain imaging system from "Quantitation and mapping of tissue optical properties using modulated imaging [5]." . . .	15
2.5	Lena image compressed via the fast Fourier transformation (FFT). The spectrogram reveals the most important components of the coefficient vector, ω . The perceptual quality of the compressed version of Lena is perceptually similar to the uncompressed version considering 95% of coefficients, ω , are discarded.	18
2.6	Image of 64x64 resolution Bernoulli measurement matrix (left) and corresponding distribution. Measurement matrix shown is 80% sparse (zero-valued).	20
2.7	Visualization of measurement vector as inner product of measurement basis and image. The measurement vector, g , is expressed as the inner product between the measurement matrix, Φ , and scenery, x . The Lena image, x , can also be expressed in terms representation basis, Ψ , and coefficients, ω . . .	21
2.8	Coherence of Bernoulli and DCT basis pair. Random measurements are more incoherent with the DCT basis with increasing dimensionality.	23

2.9	Diagram of digital micromirror device states left and orientation of mirrors on chip right.	25
2.10	Images of Bernoulli measurement matrices that are 80% sparse. The resolution of image (a) is 32x32, (b) 64x64, and (c) 128x128.	26
2.11	Schematic of single pixel camera setup capturing modulated light field from an SFDI instrument. The digital micromirror device (DMD) shown projects measurement matrices like the ones shown in 2.10.	27
2.12	Random spike signal recovered from least squares (L2) and basis pursuit (L2). Most of the energy is preserved in the basis pursuit solution, whereas the least squares solution is unable to find the sparse solution.	28
2.13	Lena image (128x128 resolution) recovered from 20 percent of samples. The least squares solution is noticeably noisier than the basis pursuit solution.	29
2.14	Lena expressed in terms of sampled and unsampled coefficients. The sampled coefficients are the top 5% most significant coefficients. The unsampled coefficients are, mostly, high frequency components.	30
2.15	Probability density function of normal distribution. Notice, as the variance decreases the distribution becomes more concentrated around the mean ($\mu = 0$).	31
2.16	Diagram of SFDI system that implements SPC for detection [17].	34
3.1	Diagram and component list of single pixel spatial frequency domain imaging (spSF DI) instrument used to measure optical properties of brain tissue simulating phantom.	38
3.2	SPC SFDI prototype constructed in lab. The SPC DMD II reflects backscattering light from the Turbid Media the Coupling Optics, which focuses light onto the active area of the Detector.	39
3.3	Binary composition of SFDI pattern. Bit 1 indicates the most significant bit.	40
3.4	First 100 samples from measurement vector collected from spSF DI instrument. For each measurement, 1000 samples were recorded then averaged to account for the rapid movement of projection DMD.	41
3.5	Image of open-SFDI system constructed in lab to compare against prototype SPC SF DI setup.	42
3.6	Optical property quantification of brain simulating phantom using camera and single pixel camera based spatial frequency domain instruments.	43
3.7	Optical property quantification of brain simulating phantom using camera and single pixel camera based spatial frequency domain instruments.	44
4.1	Convolutional neural network implemented to achieve single pixel imaging frame rates. The network encodes the input image with a set of learned Bernoulli measurement matrices. Following encoding, a decoding network transforms the latent space representation (or g) into an image.	46
4.2	Optical property maps of brain tissue simulating phantoms imaged in our lab. The left and right center regions are liquid brain tissue simulating phantoms (noise outside perimeter from not imaging phantom).	48

List of Symbols

$f - NIRS$	functional near infrared spectroscopy
Hb	deoxygenated hemoglobin
HbO	oxy-hemoglobin concentration
HbT	total hemoglobin concentration
SNR	signal to noise ratio
μ_a	absorption coefficient
μ_{tr}	transport coefficient
μ_{eff}	total effective attenuation
μ'_s	reduced scattering coefficient
k_x	spatial frequency of photon density wave
α	phase shift of photon density wave
d	diffuse reflectance
d	diffuse reflectance of modulated photon density wave
AC	modulated photon density wave
AC,ref	reference modulated photon density wave
ϵ	extinction coefficient
λ	wavelength of light
a	albedo coefficient
a'	reduced albedo coefficient
C	molar concentration
C_{HbO}	molar concentration of oxygenated hemoglobin
C_{Hb}	molar concentration of deoxygenated hemoglobin
VIS	visible spectrum of light
NIR	near-infrared light
IR	infrared light
UV	ultraviolet light
nm	nanometer
ψ	fluence rate
ω	coefficient vector
ω_s	sampled coefficients
ω_e	error coefficients
ω_n	noise
Ψ	representation basis
Φ	measurement basis
Θ	transformation basis
K	number of measurements
K	total number of measurements
g	measurement vector
q	power per unit area
σ^2	variance of normal distribution

<i>RVM</i>	relevance vector machine
<i>LED</i>	light emitting diode
<i>ACL</i>	aspheric condenser lens
<i>ADL</i>	aspheric diverging lens
<i>fft</i>	fast fourier transformation
<i>ROI</i>	region of interest
<i>LUT</i>	look up table
<i>StO</i>	oxygen saturation
<i>CW</i>	continuous wave
<i>FM</i>	frequency modulated
<i>APD</i>	avalanche photodiode
<i>SPCM</i>	single photon counting module <i>ADC</i>
analog to digital converter	
<i>SPC</i>	single pixel camera
<i>CCD</i>	charge-coupled device
<i>sCMOS</i>	scientific complementary metal-oxide-semiconductor
<i>CMOS</i>	complementary metal-oxide-semiconductor
<i>SFDI</i>	spatial frequency domain imaging
<i>TD</i>	time domain
<i>SPI</i>	single pixel imaging
<i>SFDI</i>	spatial frequency domain imaging
<i>spSFDI</i>	single pixel spatial frequency domain imaging
<i>SPCSFDI</i>	single pixel camera spatial frequency domain imaging
<i>SLM</i>	spatial light modulator
<i>DMD</i>	digital micromirror device
<i>SPECT</i>	single photon emission computed tomography
<i>MTF</i>	modulation transfer function
<i>JPEG</i>	joint photographic experts group
<i>TIFF</i>	tagged image file format
<i>DCT</i>	discrete cosine transformation
<i>UINT8</i>	8-bit unsigned integer

Acknowledgment

I would like to take this opportunity to thank my professor for introducing me to optical imaging. It has been a wonderful privilege to develop state of the art instruments, which I believe one day, will revolutionize medical imaging. Especially, I would like to mention the gratitude I have for my parents support and patience throughout my academic career.

Dedicated to

My family and mentors who have supported my dreams and academic endeavors.

Introduction

This section will provide the main motivation for this thesis, discuss about limitations in the current approach, and the need for single-pixel approach for imaging of neurological disease such as Alzheimer's disease with the context of the potential impact for clinical and preclinical research.

1.1 The Need for Imaging Contrasts for Clinical and Pre-clinical Research

World-wide, more than 35 million people are diagnosed with Alzheimer's disease with 5.5 million cases in the United States. With the odds of people over 85 developing Alzheimer's being 1 in 3, it poses an issue with the aging demographic in the United States. According to the census, the United States anticipates, by the mid-century, that the number of cases will increase from 13.2 to 16.0 million [13].

The pathogenesis of Alzheimer's disease isn't well understood, but its pathology is characterized by amyloid angiopathy, loss of neurons and white matter, inflammation, and oxidative damage to nerve tissue [13]. These changes can be detected by imaging modalities with contrasts of cell/neuronal density, blood flow, and oxygenation. Detecting these changes in the brain with medical imaging modalities, such as single-photon emission computed tomography (SPECT) and magnetic resonance imaging, is very expensive, uses

harmful radiation (in the case of SPECT), and takes a relatively long time to perform. As I will detail for the motivation for optical imaging, it can provide these contrasts non-contact, fast, and noninvasively. This can be highly suitable for bedside monitoring as well as for preclinical research with animal studies. Preclinical studies can provide systematic, rigorous research on establishing these imaging contrasts as biomarkers for both early diagnosis and therapy response monitoring of Alzheimer's disease for fast clinical translation.

1.2 Optical Absorption and Scattering Contrasts in Diffuse Optical Imaging for Brain Tissue Characterization

Living tissue is a highly scattering medium like milk or the clouds in the sky, not transparent like water, and can cause photons to have a multi-scattering (diffuse) before reaching a detector. Optical imaging measures two intrinsic physical contrasts, optical absorption, μ_a cm^{-1} and scattering μ'_s cm^{-1} . During this photon diffusion process, some photon can get absorbed from the tissue chromophores (absorbers) like hemoglobin in blood. Elastic scattering (no energy loss during scattering process) leads to deviations of the original photon paths, and photons scatter out of detector viewing angle due to limited acceptance angle of the detectors. Thus, light attenuates due to direct absorption loss and scattering loss. Tissue scattering dominates compared to absorption, which means there is a high chance that there will be more scattering events than absorption events, allowing light to probe thick tissues like brain. Figure 1.1 illustrates photons propagating in multi-scattering medium. Tissue scattering is wavelength dependent, described by Mie scattering, $\mu'_s = a\lambda^{-b}$, where a indicates the scattering number, related to number of scatterers, and b represents the scattering power related to the size of the scatterers. μ'_s is a measure of photons scattering off

organelles such as cells and neurons.

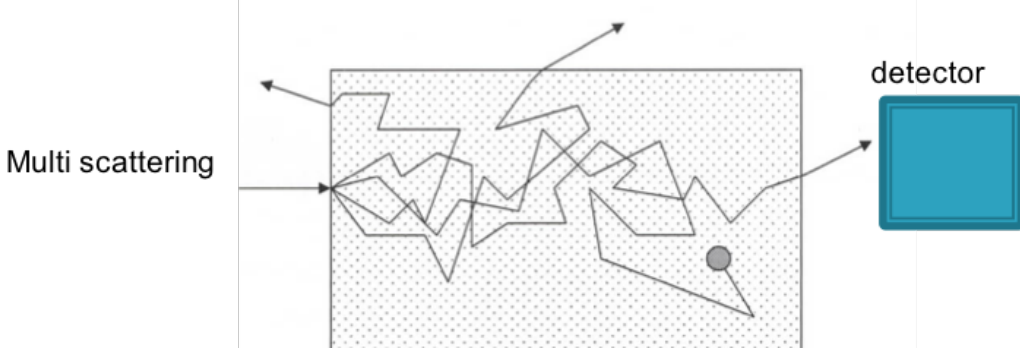


Figure 1.1: Photons highly scatter or get absorbed in living tissue like brain before reaching to photon detector.

Optical absorption is a measure of the amount of light attenuation caused by chromophores present in tissue. Optical absorption, μ_a , is formally defined as the product of the molar concentration, $C[mol/L]$, and the molar extinction coefficient, $\epsilon^{-1}[M]$, $\mu_a = C\epsilon$. Optical absorption and scattering are functions of wavelength. In near-infrared (NIR) light window of wavelengths between 650nm to 900nm, the main absorbers are oxy- and deoxy-hemoglobin (HbO, Hb). Therefore, one needs to compute the sum of the absorption coefficients to get the overall optical absorption of the brain, $\mu_a(\lambda) = \epsilon_{HbO}(\lambda)C_{HbO} + \epsilon(\lambda)C_{Hb}$. Here, ϵ_{Hb} are molar extinction coefficients of HbO and Hb at specific wavelength (λ), and these can be obtained from look-up table (LUT) obtained previously, and C represents concentrations. For in vivo imaging at clinical and preclinical settings, the physiological parameters of hemoglobin concentrations might be more desired parameters compared to physical parameters of absorption and scattering parameters. The oxy- and deoxy-hemoglobin concentrations (C_{HbO}, C_{Hb}) can be obtained minimum by two absorption measurements at two wavelengths. As Figure 1.2 indicates, molar extinction coefficient in the NIR is much lower than other wavelength regions (such as visible-VIS (400nm-700nm) and ultraviolet-UV light region (below 400nm)), thus at NIR light penetration is larger, highly suitable for brain imaging. For obtaining hemoglobin concentrations, (C_{HbO}, C_{Hb}), it is better to use one wavelength below the isosbestic point, 800nm, to have sensitivity

for deoxyhemoglobin, and one above 800nm to have sensitivity for oxyhemoglobin. The ratio of C_{HbO} to C_{Hb} is a measure of oxygen saturation. For example, pulse oximeters use red (660nm) and infrared (940nm) light to quantify oxygen saturation, a highly useful parameter indicating how much of the input (arterial) hemoglobin in the blood in the lung is oxygenated. During my thesis studies, I only had one wavelength (660nm) in my setup, thus I will focus on optical parameters rather than physiological parameters.

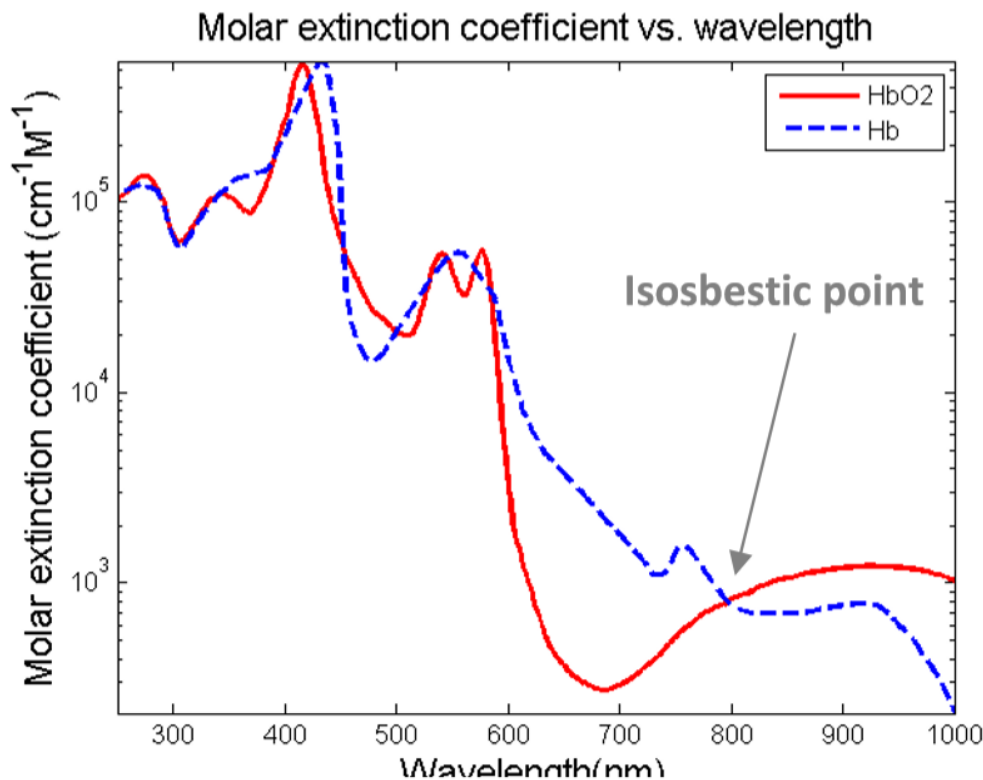


Figure 1.2: Molar extinction (absorption) coefficient of oxygenated and deoxygenated hemoglobin with respect to wavelength in brain tissue. The isosbestic point is the wavelength, which oxygenated and deoxygenated hemoglobin attenuate light equally.

These optical parameters of absorption and scattering parameters can induce optical contrasts to characterize neurological disease Alzheimer's disease. As Wilson et al. [18] demonstrated in an animal model, and summarized in Figure 1.3, the Alzheimer's group showed higher scattering parameter (possibly due to increased plaque formation), and lower

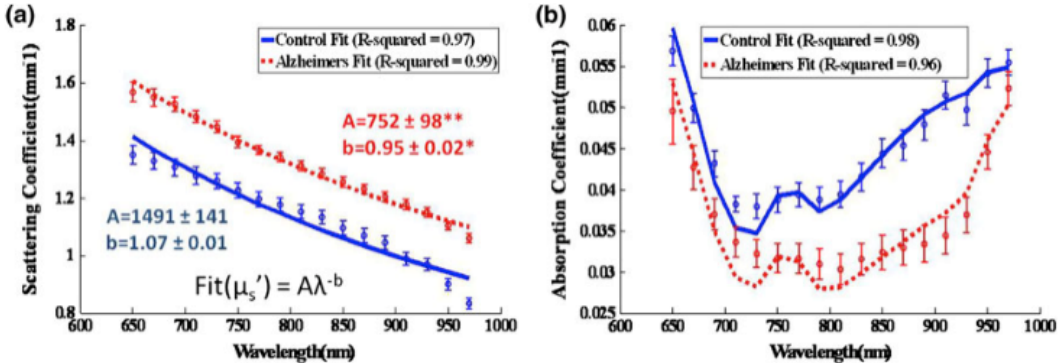


Figure 1.3: Optical scattering and absorption parameters provide contrast for Alzheimer’s disease [18].

absorption coefficient (possibly due to lower hemoglobin concentrations in the blood).

1.3 The Proposed Approach: Single-Pixel Spatial Frequency Domain Imaging for Non-contact, Wide-Field Optical Imaging

Diffuse optical devices mostly operate in the continuous wave (CW) domain, rather than the frequency (FD) or time domain (TD), due to its simplicity and cost. However, in CW it is hard to obtain both absorption and scattering parameters since the effective attenuation (μ_{eff}), which dictates how light attenuates is a combination product of the both parameters, $\sqrt{\mu_{eff}} = \sqrt{3\mu'_s\mu_a}$. Thus, any signal loss can be due to absorption, scattering, or both. Thus light absorption and scattering cannot be decoupled. As detailed in Chapter 2, modulating the light spatial frequency domain imaging (SFDI) allows quantification of both optical scattering and absorption. Most diffuse optical techniques for brain tissue characterization, such as commercially available functional near infrared spectroscopy (f-NIRS), are based on point-based spectroscopic approaches (not imaging) that utilize contact fibers for delivering and detecting light in the brain. This approach require optical probes to be in-contact

and can quantify only bulk, global average brain tissue optical properties with limited spatial heterogeneity. Recently, a localized optical imaging modality, called spatial frequency domain imaging (SFDI), has gained attention given its potential in preclinical and clinical applications as a non-contact, wide-field medical imaging instrument that is affordable and compact enough to be used for basic research in lab settings and at the bedside. Recently, SFDI demonstrated contrast in optical absorption and scattering in an Alzheimer's mouse model [10]. As Figure 1.4 clearly indicates SFDI can provide images of absolute optical absorption and scattering parameters

However, the spectral characteristics, sensitivity, and cost of cameras used in traditional SFDI have been a barrier to SFDI that is practical for the clinic. The current state of the art SFDI hardware is limited for clinical use, because the cameras used for detection are expensive and may not as sensitive as other single-pixel detectors. Moreover, most of the available scientific grade cameras are in VIS or NIR optical window (500-900nm). In some cases longer wavelengths are desired in the near IR region (greater than 1000nm), using IR cameras may not be optimal for living tissue imaging due to their higher noise (more than 500-fold) than NIR cameras. However, it is usually easier to find more sensitive and low noise single photon detectors at any wavelength windows. Thus, compared to camera-based systems, it would be easier to implement single pixel imaging for wide-range of applications.

In this thesis, a single pixel spatial frequency domain imaging (spSFDI) system and algorithms were implemented. Then, the response of the device with brain tissue mimicking phantoms is characterized. As a reference, an open source SFDI setup called “open-SFDI” is used for a comparison of the system performance. Ultimately, this approach will be a cost effective SFDI instrument that would be practical for the wide-range of applications in preclinical and clinical settings.

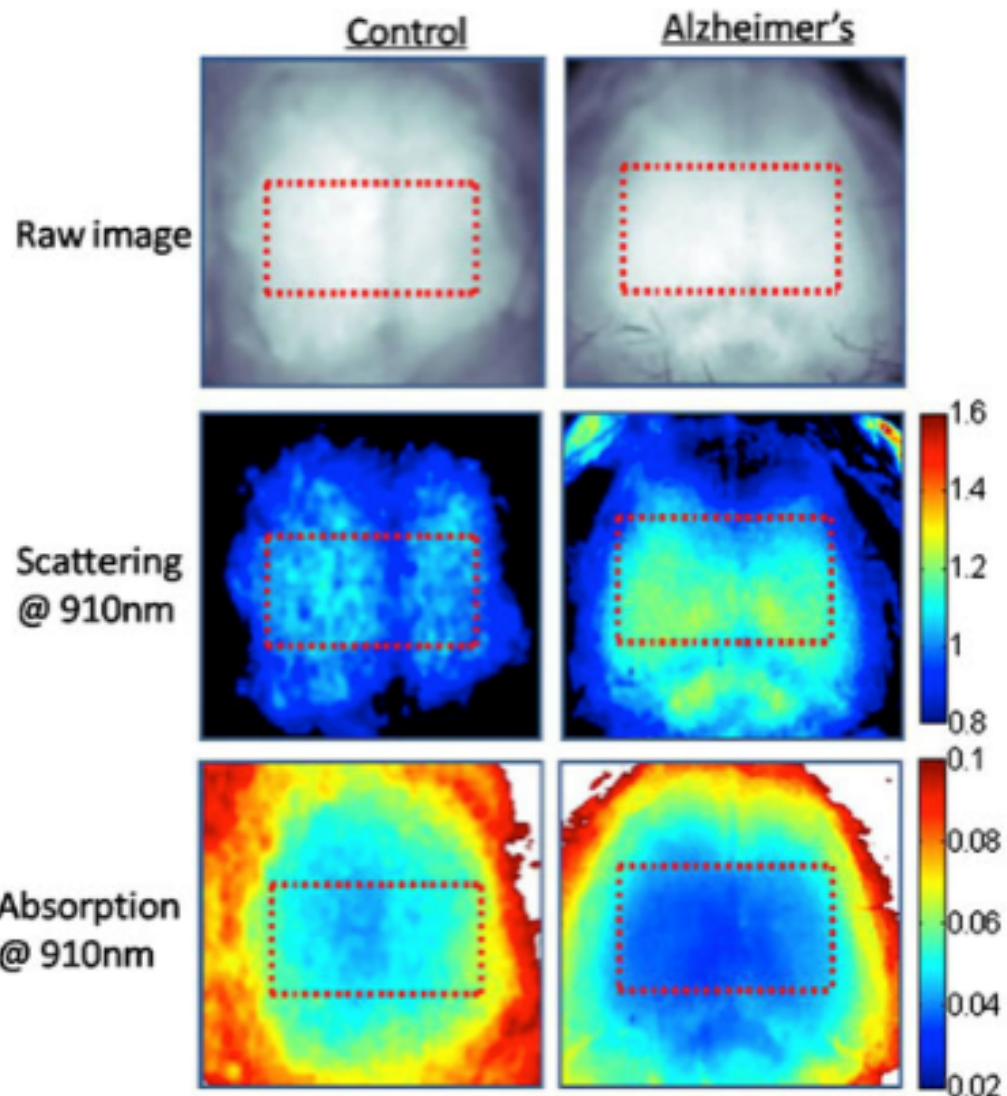


Figure 1.4: Noncontact spatial frequency domain imaging (SFDI) provides optical absorption and scattering contrasts in Alzheimer's disease [10].

Theory

This section will describe the spatial frequency domain mode in the photon diffusion domain to quantify absolute optical parameters and introduce single pixel imaging and compressed sensing methodologies as an alternative to the traditional spatial frequency domain imaging (SFDI) approach that involves two-dimensional sensors like charged coupled devices (CCDs).

2.1 Photon Diffusion in the Spatial Frequency Domain

Spatial frequency domain imaging (SFDI) is a wide-field imaging technique that quantifies optical absorption, μ_a , and reduced scattering, (μ'_s). It has advantages over point spectroscopic techniques because it can provide local maps (images) of these optical contrasts. The signals we wish to detect with SFDI are modeled as a spatially modulated photon density wave in the spatial frequency domain. In the context of light diffusion where scattering, μ'_s , is many orders of magnitude greater than absorption, μ_a , the light diffusion in a homogeneous medium can be described by a second-order photon diffusion equation:

$$\nabla^2 \varphi - \mu_{eff}^2 \varphi = -3\mu_{tr}q \quad (2.1)$$

Here, φ is the fluence rate related to measured power per unit area, q is the source illumination, μ_{eff} is the effective attenuation, related to the product of absorption and scat-

tering parameters, $\mu_{eff} = \sqrt{3\mu'_s\mu_a}$, and $\mu_{tr} = (\mu_a + \mu'_s)$ is the total attenuation of light contributed by both absorption and scattering. In the spatial frequency domain, we spatially (here sinusoidal illumination) modulate the light source to project light pattern that is normal to the plane of incidence:

$$q = q_0(z)\cos(k_x x + \alpha), \quad (2.2)$$

where q_0 is the power at depth z , the spatial frequency is $k_x = 2\psi_x$ and α represents phase shift offset in radians. If the media's response to the source illumination is proportional to the input intensity, the sinusoidal pattern reflecting from the media will have the same spatial frequencies. Therefore, we can model the measured light intensity or fluence rate, φ , reflecting from the media with the same frequency as the source, q :

$$\varphi = \varphi_0(z)\cos(k_x x + \varphi)\cos(k_y y + \beta) \quad (2.3)$$

Substituting Equations 2.1 and 2.2 into 1 yields a one dimensional photon diffusion equation for the fluence rate as a function of depth z , which is the Helmholtz type differential equation:

$$\frac{d^2}{dz^2}\varphi_0(z) - \mu'_{eff}^2\varphi_0(z) = -3\mu_{tr}q_0(z), \quad (2.4)$$

This diffusion Equation (2.4) implies that the solution for fluence rate can be modeled as an exponentially-damping signal with respect to depth z with a decay rate of μ'_{eff} , which is defined as the effective attenuation,

$$\mu'_{eff} = \sqrt{\mu_{eff}^2 + k_x^2}. \quad (2.5)$$

Equation 2.6 indicates that the decay rate depends on the usual effective attenuation (μ_{eff}^2) for the continuous wave (CW) case when there is no modulation, with an addi-

tional term of spatial frequency modulation, k_x^2 . Thus, the effective attenuation increases with spatial frequency, and higher frequencies are more attenuated (tissue acts as low-pass filter). Thus, higher frequencies are more sensitive to superficial tissue while lower frequencies probe deeper tissue. Since absorption length ($1/\mu_a \sim 100\text{mm}$) is much larger than scattering length ($1/\mu'_s \sim 1\text{mm}$) higher frequencies are more sensitive to scattering (photons definitely scatter at the illuminated superficial region). From this, we can also infer that spatial modulation allows depth sectioning (or depth sensitivity), with the effective penetration depth can be defined as $\delta'_{eff} = 1/\mu'_{eff}$. Following the derivation from “Quantitation and mapping of tissue optical properties using modulated imaging” [5], the diffuse reflectance (the measured reflected light) can be obtained as:

$$R_d(k) = \frac{3Aa'}{(\mu'_{eff}/\mu_{tr} + 1)(\mu'_{eff}/\mu_{tr} + 3A)'}, \quad (2.6)$$

where $a' = \mu'_s/\mu_{tr}$ is the reduced albedo and $A = (1 - R_{eff})/2(1 + R_{eff})$ is the proportionality constant. Here, n is the refractive index of tissue and $R_{eff} = 0.0636n + 0.668 + (0.710/n) - (1.440/n^2)$ is the effective reflection coefficient. Thus, one can simulate photon diffuse reflectance with respect to different spatial frequencies for different cases of optical parameters by using this simple and fast analytical solution via MATLAB. The optical properties, μ_a and μ'_s , can be recovered by fitting this model to the experimental data.

2.1.1 Projection and Demodulation of Spatially Varying Modulated Light

In the previous section, the diffusion equation was solved in the spatial frequency domain. The sinusoidally varying photon density waves, described by Equation 2.3, encode the optical property information. In practice, three equally spaced phase shifted sinusoidal patterns are projected as shown in Figure 2.1.

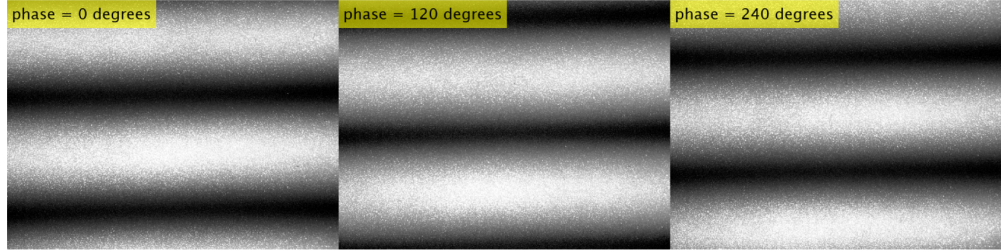


Figure 2.1: SFDI projections captured from SFDI instrument. For a single spatial frequency, f_x , there are three phases.

To recover the reflectance for a single spatial frequency, the amplitude modulation must be obtained through demodulation expressed by Equation 2.7,

$$R_{AC}(x_i, f_x) = \frac{\sqrt{2}}{3} \sqrt{[I_1(x_i) - I_2(x_i)]^2 + [I_2(x_i) - I_3(x_i)]^2 + [I_3(x_i) - I_1(x_i)]^2}, \quad (2.7)$$

where I_1 , I_2 , I_3 represent the modulated SFDI patterns like the ones shown in 2.1. Each demodulated spatial frequency corresponds to a point of the modulation transfer function (MTF) that is fit to find the optical properties. Using three-phase demodulation approach is advantageous because it allows removing common average image noise and digitization offset [6].

2.1.2 Normalized Reflectance and Optical Property Quantification

Experimental modulation amplitude, $M_{AC}(x_i, f_x)$, depends on the source intensity, the modulation transfer function (MTF) of the illumination and imaging optical system, and tissue MTF, R_d , also called diffuse reflectance of the tissue depending on the spatial frequencies:

$$M_{AC}(x_i, f_x) = I_0 MTF_{system}(x_i, f_x) R_d(x_i, f_x) \quad (2.8)$$

Since we are only interested in tissue response, R_d , one can obtain it by normalizing the measurements to a reference standard, where intensity and instrument response is assumed to be the same for both unknown and reference measurements. Thus, unknown diffuse reflectance, R_d , which contains the tissue response (and optical properties) can be written as:

$$R_d(x_i, f_x) = \frac{M_{AC}(X_i, f_x)}{M_{AC,ref}(x_i, f_x)} * R_{d,ref,pred}(f_x), \quad (2.9)$$

where R_d is the calibrated reflectance curve, M_{AC} is the MTF of the tissue, $M_{AC,ref}$ is the MTF of the reference phantom, and $R_{d,ref,pred}$ is the reflectance curve for the known reference phantom. This normalization allows eliminating absolute intensity and instrument response measurements [6]. An example of R_d curve measured from a human skin is shown in Figure 2.2.

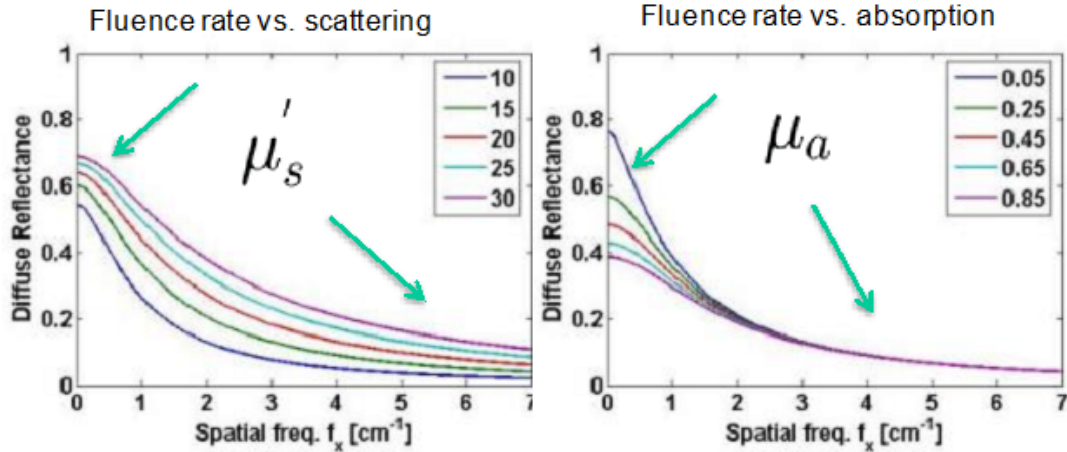


Figure 2.2: Diffuse reflectance with respect to optical absorption and reduced scattering.

Note, each pixel in a reflectance image at spatial frequency, f_x , corresponds to its own point in the reflectance curve. For example, a set of 100x100 reflectance images for x spatial frequencies would have 10000 reflectance curves.

By fitting the reflectance, R_d , curve for each pixel, the optical properties can be obtained, locally. As mentioned above, one of the main advantages of SFDI is the sensitivity

to both scattering and absorption by projecting different spatial frequencies. This can be seen clearly in Figure 2.3, where R_d , curve is plotted with respect to spatial frequencies by changing the optical parameters at a single pixel. For example, Figure 2.3 (right) shows R_d values do not change at high frequencies at different absorption coefficients. This indicates that R_d is not sensitive to absorption parameter, μ_a , but only scattering parameter, μ'_s .

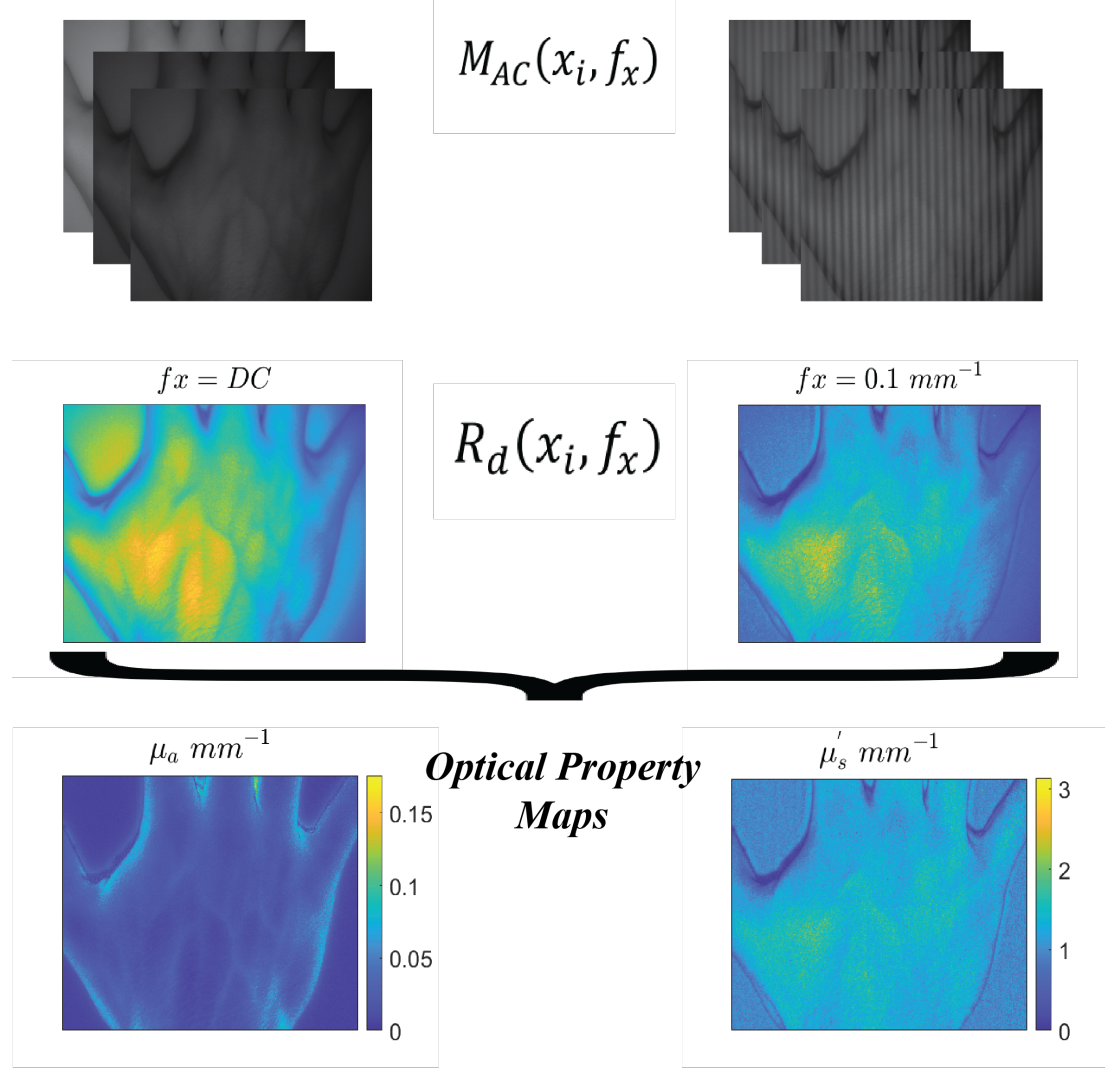


Figure 2.3: Flow chart for quantifying optical properties. In this example, there are two spatial frequencies that are demodulated and fit to obtain the optical property maps. Data provided from Open-SFDI.

Figure 2.3 (left) indicates that scattering parameters are sensitive to both high and low spatial frequencies. As mentioned before, this spatial frequency-dependent sensitivity al-

lows for accurate quantification of both μ_a and μ'_s .

There is a trade-off between the accuracy of optical property quantification and data acquisition time. Typically, three spatial frequencies at DC, low and high spatial frequency components are used to obtain accurate quantification of both μ_a and μ'_s . A least squares minimization method is used to fit R_d for each pixel to obtain the optical property maps. A flow chart of optical property map quantification is shown in Figure 10.

A diagram of a traditional spatial frequency domain imaging instrument is shown below in Figure 2.4.

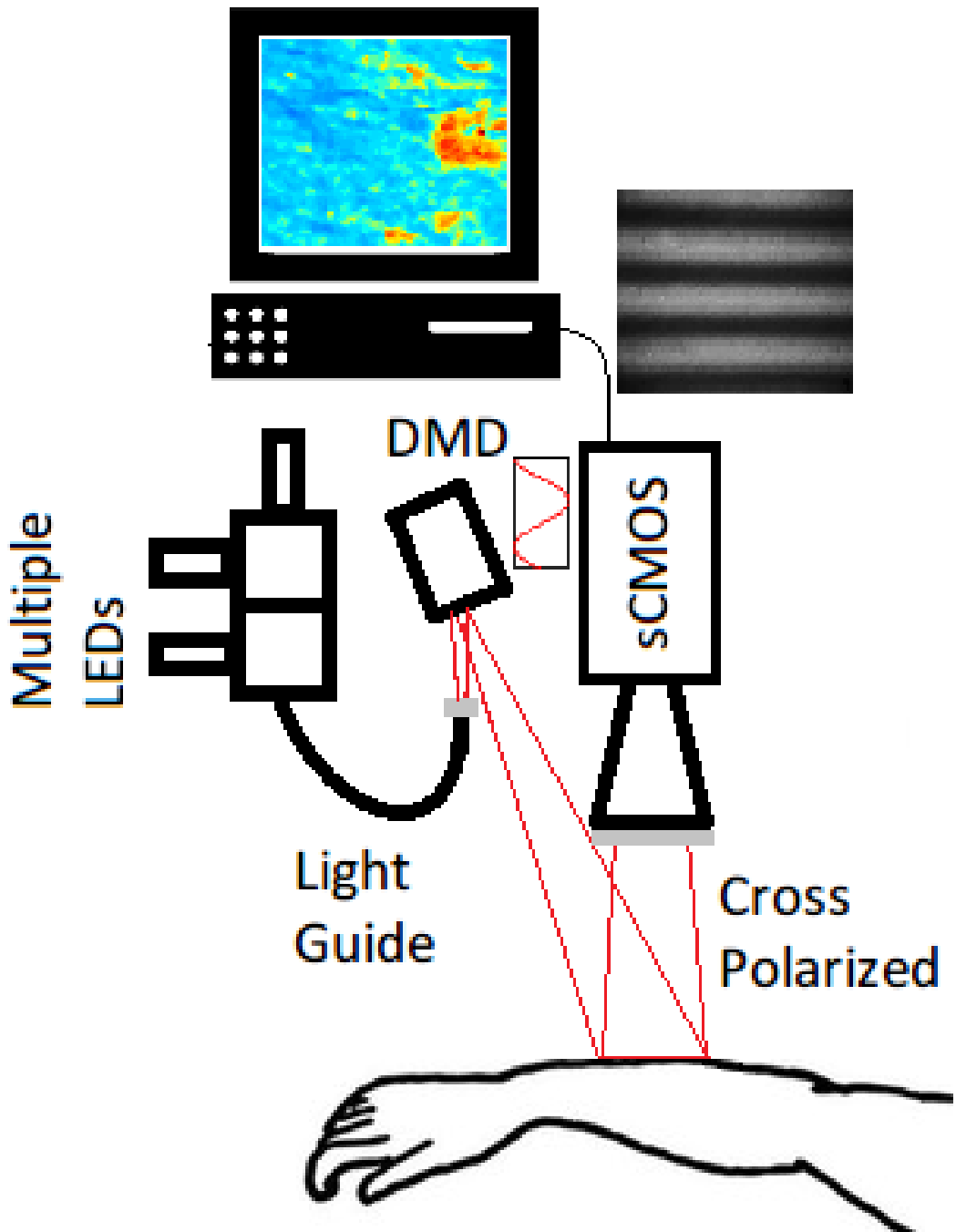


Figure 2.4: Diagram of spatial frequency domain imaging system from “Quantitation and mapping of tissue optical properties using modulated imaging [5].”

Multiple LED light at different wavelengths coupled with a light guide focused onto a spatial light modulator (SLM) that produces the sinusoidal modulation patterns. Light from DMD illuminate the tissue phantom and diffuse reflected light is measured my scientific CMOS (sCMOS) camera. Cross-polarizers eliminates specular reflection so that only photons that diffuse in the tissue are measured.

2.2 Compressed Single Pixel Imaging

Conventionally, the sampling rate must be twice the bandwidth of the signal to capture all its Fourier components dictated by the Shannon-Nyquist theorem, which is the fundamental principle behind many consumer devices such as radio receivers, visual electronics, and medical imaging devices [2]. However, with compressed sensing, sparse signals can be recovered, perfectly, from sub-Nyquist samples with high probability. This has led to compressed single pixel imaging which is the imaging modality used to capture the light field projected by our proposed SFDI instrument.

In this section, I will first describe image compression which enables compressed sensing to find a sparse representation of the diffuse light-field that is measured in SFDI. Second, the compressive sampling approach followed by the single pixel camera architecture will be described. Following the compressive measurement and single pixel camera sections, briefly, the compressed sensing framework that reconstructs images from a sub-Nyquist number of compressive measurements will be discussed. Finally, a single pixel camera based spatial frequency domain imaging instrument developed by Torabzadeh et. al. is mentioned due its heavy influence on this work.

2.2.1 Image Compression

Images captured by cameras are digitally stored as matrices, where each entry corresponds to an illuminance value. This thesis will focus on grayscale images that are represented by a 2-D matrix whose entries correspond to the illuminance of a light field at a single wavelength, λ . Furthermore, images are “flattened” from a matrix into a vector, \mathbf{x} , that is N length. Each pixel in \mathbf{x} , denoted by p , can be represented a linear combination of basis vectors,

$$\mathbf{x}(p) = \sum_{i=1}^N \psi_i(p)\omega_i. \quad (2.10)$$

The basis vectors, ψ_i , can be re-arranged into a matrix, Ψ , to more concisely write Equation 2.10 in matrix notation,

$$\mathbf{x} = \Psi\omega. \quad (2.11)$$

Transform coding is used in compressive image file formats, such as the Joint Photographic Experts Group (JPEG) and Tagged Image File Format (TIFF) standards. The idea is that natural images have a sparse representation when transformed into some representation basis, Ψ . The discrete cosine transformation (DCT), implemented in the first JPEG standard, is known to sparsely represent images in terms of sinusoidal waves with increasing frequency. By transforming the image vector, \mathbf{x} , a more efficient representation, ω , in terms of its corresponding representation basis, Ψ , is revealed. Therefore, all that is needed to represent an image is a sparse coefficient vector, ω , and the representation basis or dictionary, Ψ , that was originally used to sample the image.

In some sense, a sparsifying basis transformation reveals the most important components of signals, such as images, so less important components may be discarded without much loss in perceptual quality. For demonstration purposes, the Lena test image is com-

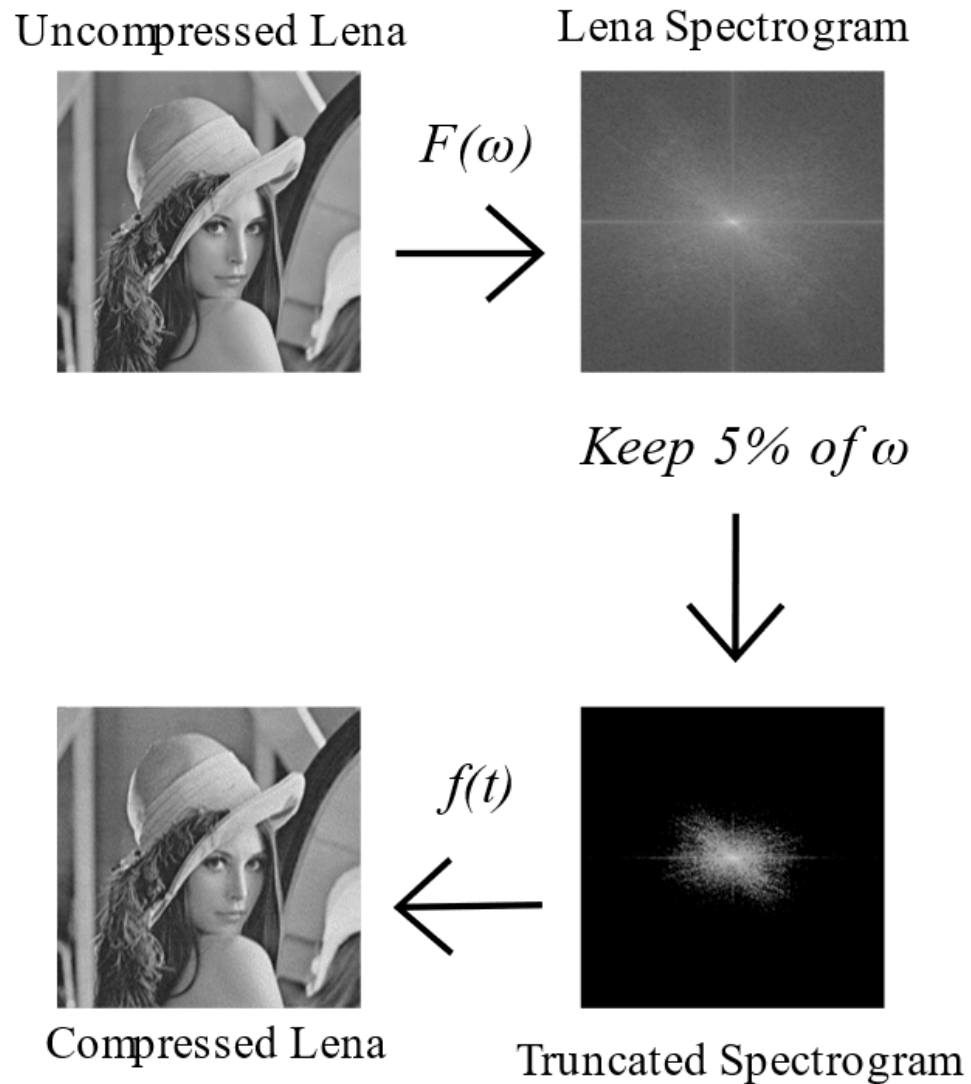


Figure 2.5: Lena image compressed via the fast Fourier transformation (FFT). The spectrogram reveals the most important components of the coefficient vector, ω . The perceptual quality of the compressed version of Lena is perceptually similar to the uncompressed version considering 95% of coefficients, ω , are discarded.

pressed via transform coding using the `fft` function in MATLAB shown in Figure 2.5.

From Figure 2.5, despite discarding a large portion of components, the perceptual quality of the compressed version of Lena is still very good, but is noticeably “fuzzier” than the uncompressed version since the high frequency components were discarded.

For compressed sensing, mentioned in Sparse Signal Recovery, the sinusoidally modulated light field projected in SFDI must have a sparse representation especially when transformed into a basis consisting of sinusoid wave functions. In theory, an image of the light field could be recovered, perfectly, from a single DCT component, ω , that corresponds to the spatial frequency of the projected SFDI pattern. However, sampling directly with a representation basis, Ψ , poses hardware limitations, so a set of measurement matrices from the measurement basis, Φ , are used to sample, instead. In previous works mentioned in the Compressed Single Pixel Spatial Frequency Domain Imaging section, a single pixel camera based SFDI instrument incorporated the same sampling method mentioned. The following section describes how compressed samples encoded with a measurement basis, Φ , can be mapped to a representation basis, Ψ , such that a sparse coefficient vector, ω , can be recovered via optimization.

2.2.2 Compressive Sampling

Considering each entry in a matrix corresponds to a byte (`UINT8`), typically, and some cameras have pixel counts in the millions, it can be memory intensive to store images. As a result of the high memory demands, it is common for consumer grade cameras to include hardware that performs some sparsifying transformation, such as the DCT, to the raw (not-compressed) image to reduce its size in memory. In some applications, the sample then compress approach may not be feasible if the dimensionality of the image is too great, which begs the question, “Why not directly acquire compressed samples?” This section describes the compressive sampling approach.

There are hardware related challenges with acquiring compressed samples directly in

the optical domain, which will be discussed in the Acquiring Compressed Samples in the Optical Domain section representation basis, but it has to do with the instrument being digital, not analog. So, it is ideal to sample the image scenery, \mathbf{x} , with a measurement basis, Φ , that can be represented by Boolean logic. Commonly used binary measurement matrices include the Bernoulli, Hadamard and Noiselet measurement matrices [4, 2]. In this work, the Bernoulli measurement matrix was used to sample.

A single Bernoulli measurement matrix and its corresponding probability distribution is shown in Figure 2.6.

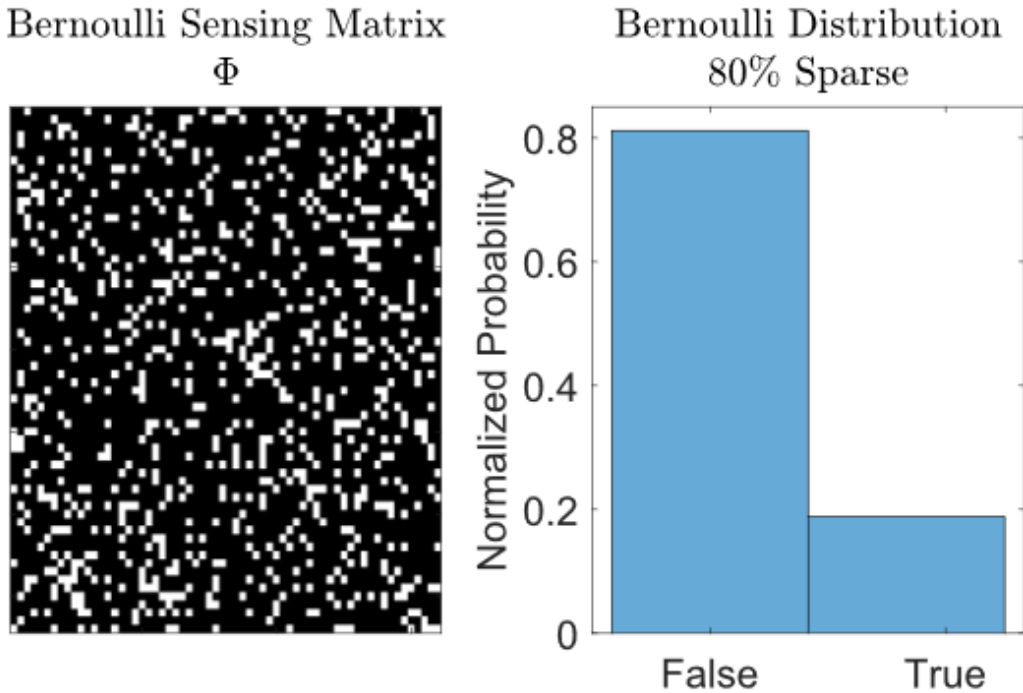


Figure 2.6: Image of 64x64 resolution Bernoulli measurement matrix (left) and corresponding distribution. Measurement matrix shown is 80% sparse (zero-valued).

An important characteristic of the Bernoulli measurement matrix is its sparsity and dimensions. As shown in the distribution, 80% of the 4096 matrix's values are false. Also, in the case of compressive sampling, the dimensionality of the measurement basis corresponds to the resolution of the recovered image, \mathbf{x} .

Compressive sampling is mathematically equivalent to the inner product of the measurement basis, Φ , and image, x ,

$$g = \Phi x. \quad (2.12)$$

The measurement vector, g , has a length, K , which is the number of measurements sampled. Each row in the measurement matrix, Φ , can be thought of as a measurement matrix like the one shown in Figure 2.6. The transformation of the measurement basis, Φ , into the representation basis, Ψ , is expressed by Θ . A visualization of the measurement vector, g , measurement basis, Φ , representation basis, Ψ , and coefficient vector, ω , is shown in Figure 2.7.

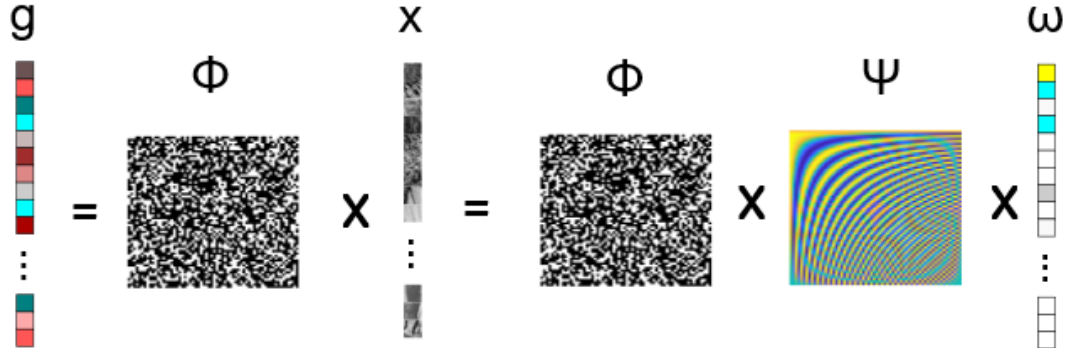


Figure 2.7: Visualization of measurement vector as inner product of measurement basis and image. The measurement vector, g , is expressed as the inner product between the measurement matrix, Φ , and scenery, x . The Lena image, x , can also be expressed in terms representation basis, Ψ , and coefficients, ω .

As shown in Figure 2.7, the measurement vector, g , is a linear combination of the measurement basis, Φ , and target image, x . Also, it can be represented as a linear combination of, Φ , some representation basis, Ψ , and vector of corresponding coefficients, ω . It is important to note that the coefficient vector, ω , is sparse and the measurement vector, g , is dense. If we were to only sample x with the representation basis, Ψ , it would be

equivalent to sampling ω directly. But, as mentioned before, the measurement basis, Φ , is easier to implement with hardware, so the acquired measurement vector, \mathbf{g} , is mapped to a representation basis, Ψ , so that a sparse solution or coefficient vector, ω , can be recovered. For compressive sampling to work, a measurement and representation basis pair must be 1.) highly incoherent and 2.) obey the restricted isometry property.

A current assumption is incoherence may be used a measure of the viability of a measurement and representation basis pair. The idea is that if a set of measure basis pairs are highly coherent, it is impossible to distinguish whether the energy in the signal comes from one basis vector or another [4]. Incoherence of a representation and sensing basis pair is the max correlation between the columns,

$$\mu(\mathbf{M}) = \max_{j < k} \frac{|\langle \mathbf{M}_j, \mathbf{M}_k \rangle|}{\|\mathbf{M}_j\|_2 \|\mathbf{M}_k\|_2} \quad (2.13)$$

The Bernoulli measurement matrix, for instance, is highly incoherent with the DCT representation basis, Ψ , especially, with increasing dimensionality. For a given measurement and representation basis pair, the coherence falls in the range between 1 and \sqrt{N} . Approximately speaking, the coherence between any fixed representation basis and random (Bernoulli) measurement matrices is $\sqrt{2\log(N)}$, where n is the number of rows and columns in the measurement/representation bases [2]. The coherence between the DCT and Bernoulli matrices with respect to dimensionality is plotted in Figure 2.8.

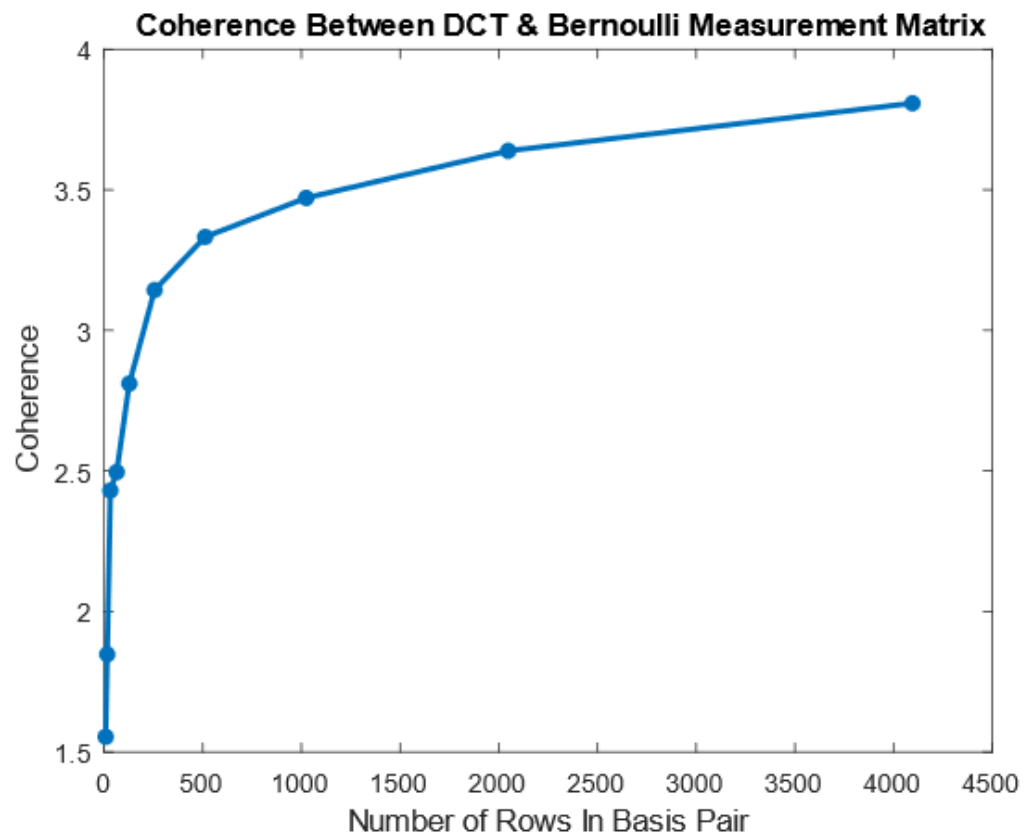


Figure 2.8: Coherence of Bernoulli and DCT basis pair. Random measurements are more incoherent with the DCT basis with increasing dimensionality.

Another property used to measure the viability and robustness of a measurement and representation basis pair is the restricted isometry property. If the measurement basis, Φ , obeys the restricted isometry property, \mathbf{x} can be recovered perfectly from an underdetermined system of equations. The restricted isometry property is formally defined in Equation (10).

$$(1 - \delta_s) \|\mathbf{x}\|_{L_2}^2 \leq \|\Phi \Psi \mathbf{x}\| \leq (1 + \delta_s) \|x\|_{L_2}^2 \quad (2.14)$$

The restricted isometry value, δ_s , is constant for a measurement basis, Φ . If δ_s is not too close to one, Φ approximately preserves the Euclidean length of \mathbf{x} . Unfortunately, RIP is difficult to compute in practice, but there are families of measurement and representation basis pairs that are known to obey this property including the Bernoulli and DCT basis pair that is used in this work [2].

2.2.3 Acquiring Compressed Samples in the Optical Domain

A single pixel camera is a relatively new camera architecture that acquires images via compressive sampling [8]. While multi-pixel cameras capture the light-field directly in the spatial domain, the single pixel camera used in our proposed instrument acquires compressed measurements via a series of random (Bernoulli) projections. In this section, the single pixel camera architecture is described.

In a broad sense, single pixel cameras are a specific type of single pixel imaging device that may be used to image visible to near-infrared light. In the case of SFDI, the signal of interest is a sinusoidally modulated light source that has a wavelength, λ , of 660 nm. To project the measurement matrices, mentioned in the compressive sampling section, a digital micromirror device (DMD) is used.

A DMD is a 2D array of bacteria-sized mirrors that can be controlled, programmatically, to project measurement matrices. The mirrors of a DMD pivot on an actuator such

that the light hitting the surface of the micromirror array can be reflected or blocked [15]. Mirrors that reflect light are considered ON, while those that block light are OFF. A simple diagram of the mirrors on a DMD chip is shown below in Figure 2.9.

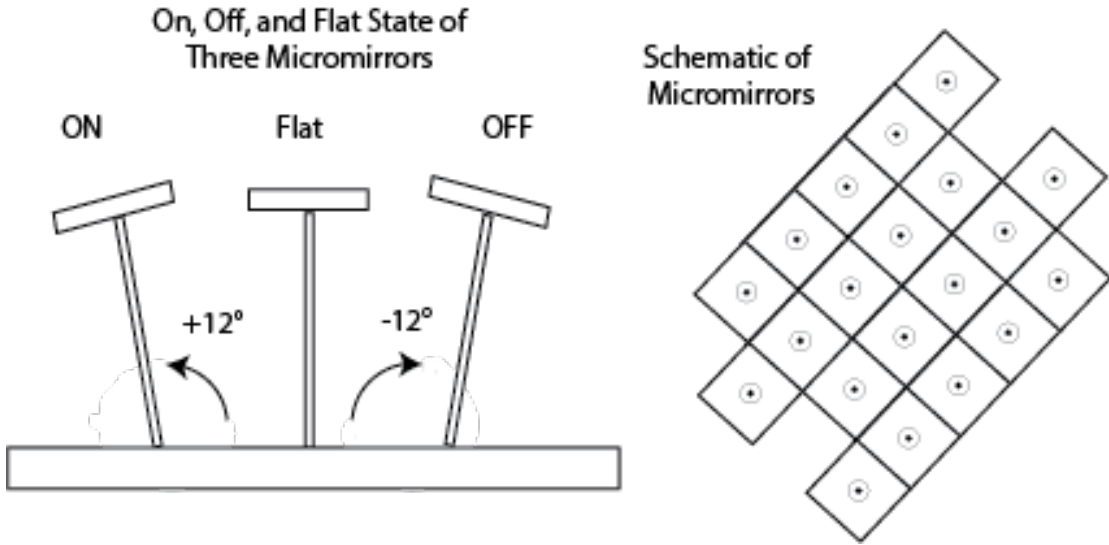


Figure 2.9: Diagram of digital micromirror device states left and orientation of mirrors on chip right.

It is common for there to be millions of mirrors on a single DMD chip, but as mentioned in the Compressive Sampling section, the dimensionality of the projected measurement matrices must not be too great. Otherwise, recovering the target image, \mathbf{x} , is infeasible. Therefore, the mirrors are binned into superpixels to reduce the dimensionality of the measurement matrices. Practical dimensions for measurement matrices are 32x32, 64x64, and 128x128. Bernoulli measurement matrices with the aforementioned dimensions are shown in Figure 2.10.



Figure 2.10: Images of Bernoulli measurement matrices that are 80% sparse. The resolution of image (a) is 32x32, (b) 64x64, and (c) 128x128.

The white pixels in 2.10 represent the ON or true state while the black pixels represent the OFF or false state. Measurement matrices, like the Bernoulli measurement matrices shown in Figure 2.10, are streamed to a DMD control board, sequentially, in a single pixel camera setup like the one shown in 2.11 to optically encode some target scenery. In the case of SFDI, the target scenery is a spatially modulated light field.

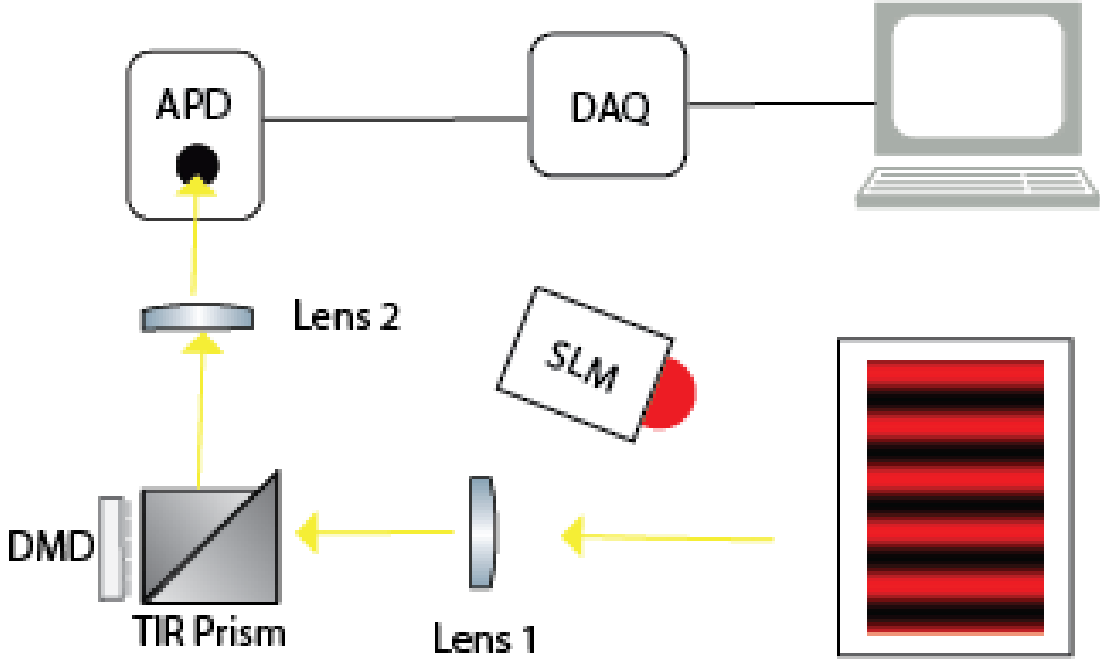


Figure 2.11: Schematic of single pixel camera setup capturing modulated light field from an SFDI instrument. The digital micromirror device (DMD) shown projects measurement matrices like the ones shown in 2.10.

In Figure 2.11, the spatial light modulator (SLM) illuminates the target scenery with an SFDI pattern. Light reflecting off the target image, x , is then focused onto the DMD with Lens 1. The DMD projects the measurement basis, Φ , in the optical domain by selectively reflecting or blocking light into Lens 2, which is then focused onto the active area of an avalanche photodiode (APD). The data acquisition device (DAQ) measures the voltage signal emitted by the APD to acquire a measurement from a measurement matrix in the measurement basis, Φ . The process repeats for each measurement matrix, ψ_i , until the desired K number of measurements are acquired for image reconstruction.

2.2.4 Sparse Signal Recovery

One of the goals of compressed sensing is to find sparse solutions to under-determined systems of equations that generally have an infinite number of solutions. By using a sparsity promoting criterion, a sparse solution can be found if the restricted isometry property holds,

the measurement and representation basis pairs are highly incoherent, and the signal of interest is sparse in some domain. By minimizing

$$\hat{x} = \arg \min \|\mathbf{x}'\|_1 \text{ such that } \Phi \Psi \mathbf{x}' = \mathbf{g}, \quad (2.15)$$

\mathbf{x} can be recovered perfectly if it is truly sparse in the representation basis, Ψ , with $K \ll N$ measurements. Conveniently, convex functions reduce to a linear program known as basis pursuit, so that the problem is only $M \leq O(K \log(N/K))$ to solve [3]. In Figure 2.12, a random, sparse signal is recovered using the least squares (L2) and basis pursuit (L1) methods.

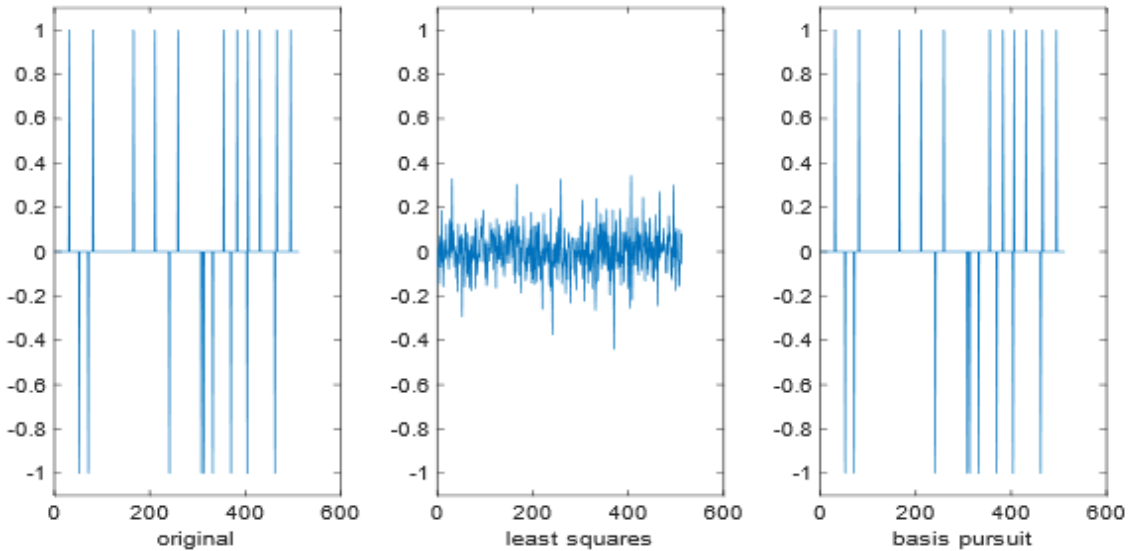


Figure 2.12: Random spike signal recovered from least squares (L2) and basis pursuit (L2). Most of the energy is preserved in the basis pursuit solution, whereas the least squares solution is unable to find the sparse solution.

Images can be described as having mostly smooth surfaces punctuated by sharp edges. The smooth surfaces are efficiently represented by the DC and low frequency components in Fourier space, while the sharp edges correspond to a few, less significant higher frequency components. Therefore, most of information in an image is encapsulated by a few Fourier terms, which the sparsity promoting criterion (L1) can find. As an example, Lena

is recovered from both the least squares and basis pursuit methods shown in Figure 2.13.

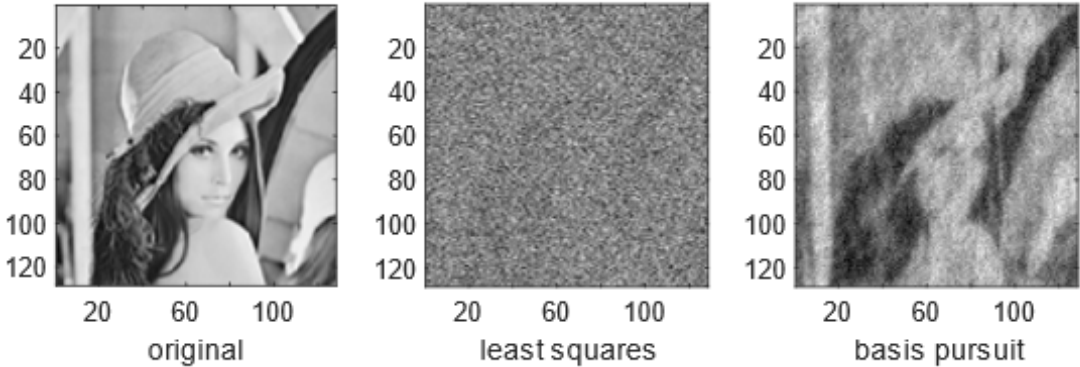


Figure 2.13: Lena image (128x128 resolution) recovered from 20 percent of samples. The least squares solution is noticeably noisier than the basis pursuit solution.

With a 20% compression ratio, the reconstruction of Lena is noticeably worse in the least square's solution, which utilizes the L2 criterion, compared to the Basis Pursuit solution.

The reconstruction methods described, so far, find a point estimate of the coefficients in the vector ω . The issue with this approach to recovering ω , known as the frequentist approach to statistics, is that the uncertainty of the coefficient vector, ω , is unknown. Because each pixel in an image corresponds to a feature, images tend to be very large in dimensionality which is the reason machine vision is a challenging problem in engineering. For very high dimensional spaces, such as images, Bayesian methods tend to work very well when the number of features is much greater than the number of observations and apriori assumptions can be made about the signal i.e. sparsity.

The Bayesian approach to compressed sensing treats each coefficient in the vector, ω , as a random variable with density function, so that the confidence of each coefficient's value can be used to update their weight or influence in a model that represents an image vector, \mathbf{x} . The rest of this section will cover the Bayesian compressed sensing which is the approach used in this work to recover the image vector, \mathbf{x} , from compressive measurements, \mathbf{g} .

When data is scarce and an apriori assumption can be made about the data, the Bayesian

approach to statistics is useful for creating robust models. In the case of sparse signal recovery, the apriori assumption is that the image, \mathbf{x} , we wish to recover is sparse when projected onto a representation basis, Ψ . So, it is reasonable to assume apriori that the component, ω , are mostly zero. The Bayesian framework is briefly described in the following section.

If the image, \mathbf{x} , is compressible in the basis, Ψ , then $K \ll N$ coefficients are needed. However, most signals, like images, are not perfectly sparse in some representation basis, Ψ , but have many insignificant components. All unsampled or insignificant components, ω_e , model the noise introduced from unsampled non-zero basis components. Returning to the Lena example in Figure 2.13, the sampled components, ω_s , can be thought of as the most significant components and the ω_e coefficients are the terms that are excluded as shown in Figure 2.14.

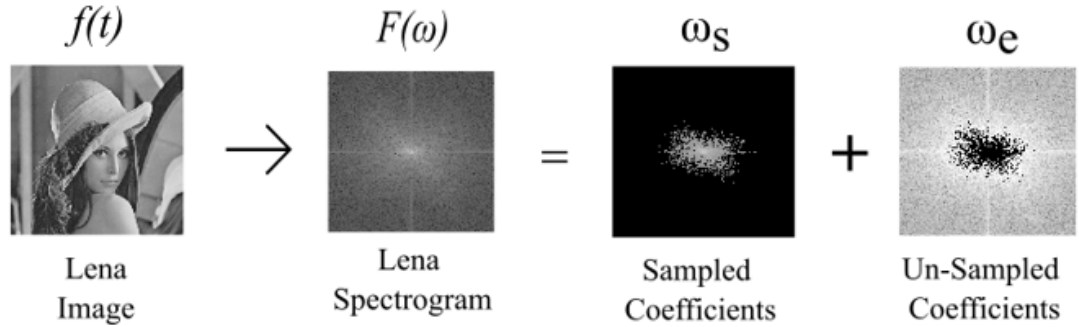


Figure 2.14: Lena expressed in terms of sampled and unsampled coefficients. The sampled coefficients are the top 5% most significant coefficients. The unsampled coefficients are, mostly, high frequency components.

The measurements in \mathbf{g} are acquired through random sampling (Bernoulli measurement matrices), so the error caused by sampling, \mathbf{n}_m , may be approximated as a zero-mean Gaussian for large $N-K$ because of the central limit theorem. Furthermore, the measurement noise introduced into the system through sampling, \mathbf{n}_m , can be represented as a zero-mean Gaussian distribution as well. Therefore, the total noise introduced into the

measurement vector, \mathbf{g} , can simply be expressed as \mathbf{n} :

$$\mathbf{g} = \Phi\Psi\omega = \Phi\omega = \Phi\omega_s + \mathbf{n}_e + \mathbf{n}_m = \Phi\omega_s + \mathbf{n} \quad (2.16)$$

The probability distribution of a single component in \mathbf{n} can be viewed as Gaussian with zero-mean and unknown variance since both noise sources, \mathbf{n}_e and \mathbf{n}_m , are Gaussian as well. In practice, the entire vector of components, ω , of the representation basis, Ψ , is considered and the unsampled components, ω_e , are simply set to zero in ω . A plot of the Gaussian probability density function with respect to various standard deviations is shown in Figure 2.15.

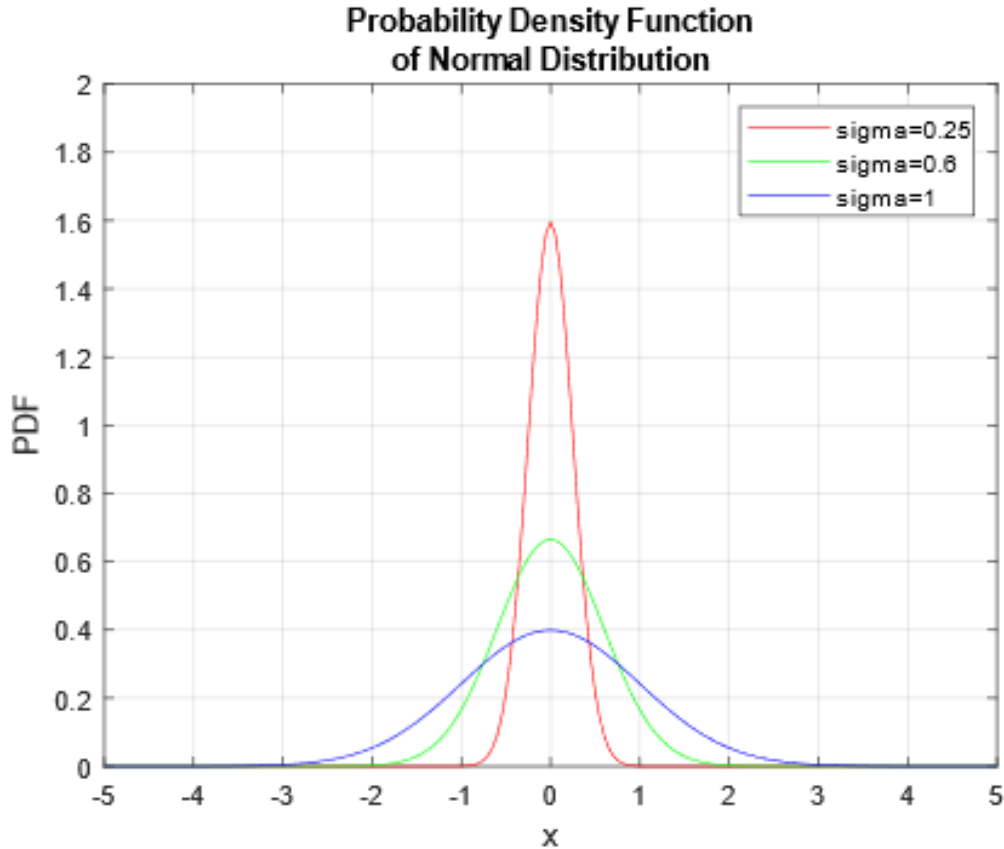


Figure 2.15: Probability density function of normal distribution. Notice, as the variance decreases the distribution becomes more concentrated around the mean ($\mu = 0$).

As mentioned earlier, one of the advantages of the Bayesian approach to statistics is the certainty of the components, ω , can be quantified. The likelihood function of the measurement vector, \mathbf{g} , is Gaussian with zero-mean and unknown variance, σ^2 ,

$$p(\mathbf{g}|\omega, \sigma^2) = (2\pi\sigma^2)^{-K/2} \exp\left(-\frac{1}{2\sigma^2} \|\mathbf{g} - \Phi\omega\|^2\right) \quad (2.17)$$

The maximum likelihood estimates of ω correspond to least-squares regression under the assumption that the total noise introduced in the system can be modeled as a zero-mean Gaussian with unknown variance. Maximum-likelihood estimation of ω and σ^2 will generally lead to severe overfitting, so a sparsity promoting prior is considered over ω , which is a zero-mean Gaussian distribution:

$$p(\omega|\alpha) = \prod_{i=1}^N \mathcal{N}(\omega_i|0, \alpha_i^{-1}) \quad (2.18)$$

where α_i is the precision (inverse-variance). The posterior over the weights is then obtained from Bayes' rule:

$$p(\omega|\mathbf{g}, \alpha, \sigma^2) = (2\pi)^{-(N+1)/2} \left| \sum \right|^{-1/2} \exp\left\{-\frac{1}{2}(\omega - \mu)^T \sum^{-1}(\omega - \mu)\right\}, \quad (2.19)$$

with

$$\sum = (\Phi^T \mathbf{B} \Phi + \mathbf{A})^{-1}, \quad (2.20)$$

and

$$\mu = \sum \Phi^T \mathbf{B} \mathbf{g}, \quad (2.21)$$

where $A = \text{diag}(\alpha_0, \alpha_1, \dots, \alpha_N)$ and $B = \sigma^{-2}I_N$. By integrating out the weights, the

marginal likelihood for the hyperparameters is

$$p(\mathbf{g}|\alpha, \sigma^2) = (2\pi)^{-N/2} |\mathbf{B}^{-1} + \Phi \mathbf{A}^{-1} \Phi^{-1}|^{-1/2} \exp\left\{-\frac{1}{2} \mathbf{g}^T (\mathbf{B}^{-1} + \Phi \mathbf{A}^{-1} \Phi^T)^{-1} \mathbf{g}\right\}. \quad (2.22)$$

Ideally, the hyperpriors, α and σ^2 , would be integrated out as well, but such marginalization cannot be performed in closed-form here, so the marginal likelihood of the hyperpriors is optimized instead which is essentially the type II maximum likelihood method. For more details on optimizing the hyperparameters, the reader is encouraged to refer to [11].

The algorithm used in this work to reconstruct the image vector, \mathbf{g} , from compressive measurements, \mathbf{g} , and representation basis, Φ , is referred to the fast relevance vector machine (fast-RVM). Fast-RVM achieves faster run-time and increases sparsity by dynamically adding and deleting columns from the transformation matrix, Θ . The reader is encouraged to read [11] for more information. The fast RVM algorithm used to recover the images in this thesis is written in MATLAB and available via open-source [16].

2.2.5 Compressed Single Pixel Spatial Frequency Domain Imaging

Prior to this work, Torabzadeh, et al., demonstrated real-time, single pixel camera based SFDI with optical property map acquisition rates of 12 Hz [17]. An important difference to note between the CCD based SFDI setup, shown in Figure 2.4, and single pixel camera based instrument, shown in Figure 2.4, is that a film mask is used to modulate the light source instead of a DMD. The complications associated with using a DMD SLM has to do with the SLM being digital, not analog. To provide clarification to the reader, a brief description of a SPC based SFDI system, originally proposed by Torabzadeh, et al., is described along with a diagram of the setup shown in Figure 2.16.

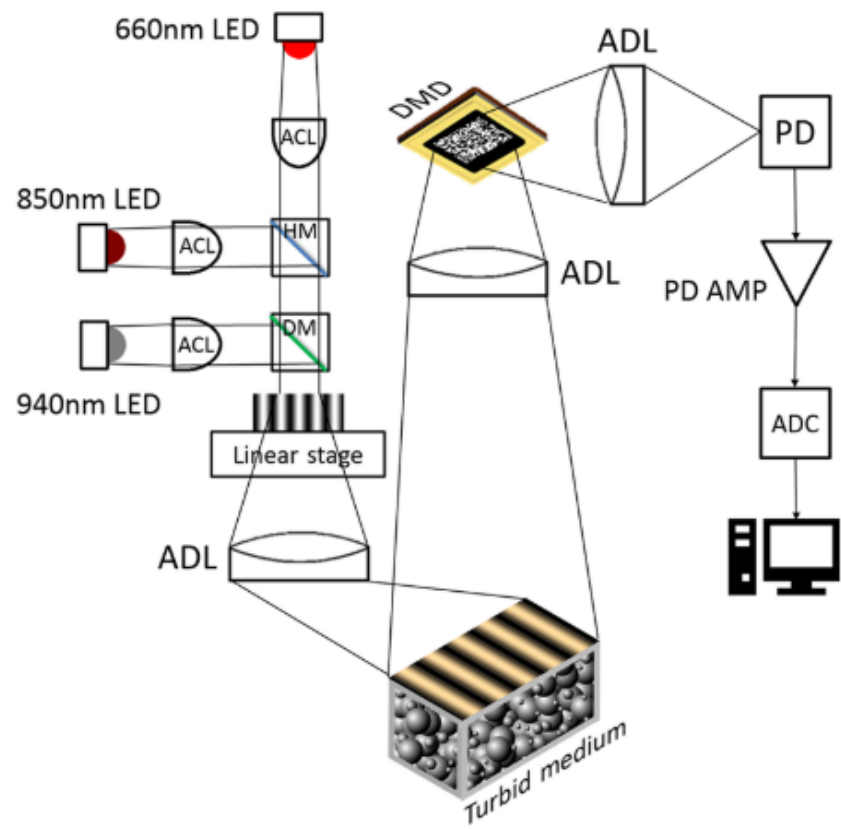


Figure 2.16: Diagram of SFDI system that implements SPC for detection [17].

In Figure 2.16, the LEDs shine light through an aspheric condenser lens (ACL), which collimates the light before it passes through a linear stage. The linear stage is simply a film mask that modulates the source LED. The modulated light that is projected onto the turbid media scatters inside the media, which is the reason why the SFDI pattern is visible. To cover the entire surface of the media with modulated light, an aspheric diverging lens (ADL) is placed in-between the linear stage (film mask) and turbid media. Backscattered light is then focused on to the surface of a DMD with a lens, which optically encodes the image. The light reflecting from the DMD chip is focused onto the surface of an avalanche photodiode (APD), so that compressive measurements can be collected. A data acquisition device (DAQ) measures the voltage signal emitted by the operational amplifier from the APD, which is logged an entry in the measurement vector, \mathbf{g} . Once the measurement is logged, a computer signals the DMD to project another measurement matrix and the process described repeats until all measurements are collected for a single SFDI pattern. Once the measurements are collected, another SFDI pattern is projected onto the media until all data is acquired. After data collection, compressed sensing algorithms, mentioned in the Sparse Signal Recovery section, are used to reconstruct the reflectance images, which are used to quantify optical property maps.

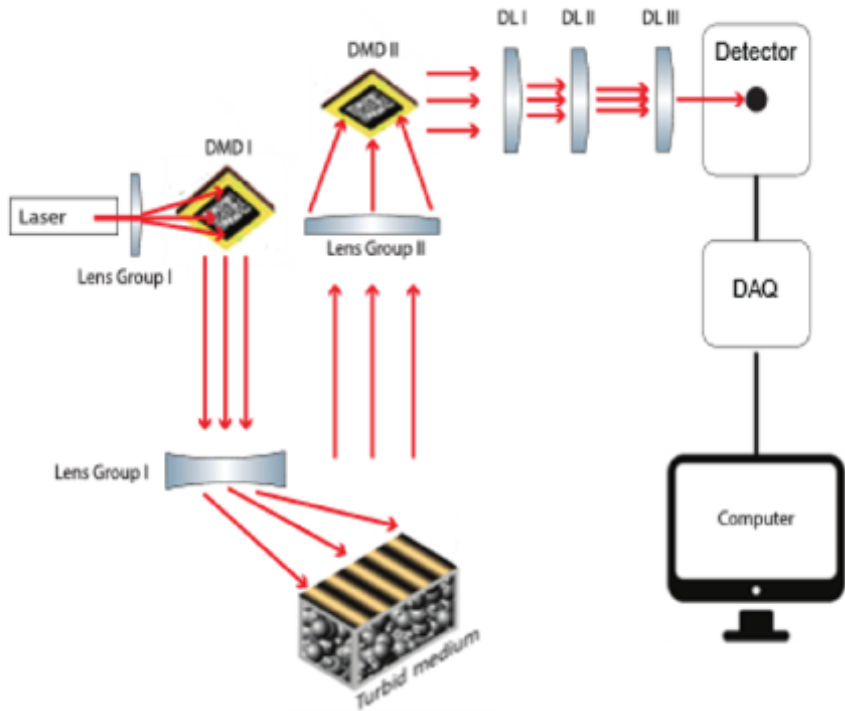
Experiment Methods and Validation

In this chapter experimental details are presented. Then, to explore the feasibility of SPC based SFDI, the optical properties of a brain tissue simulating phantom with unique optical contrast is imaged with the proposed single pixel spatial frequency domain imaging (spSFDI) instrument and a traditional, multi-pixel camera based SFDI setup. The results suggest spSFDI is comparable to a traditional SFDI instrument.

3.1 Single Pixel Spatial Frequency Domain Imaging Instrument

Single pixel spatial frequency domain imaging (spSFDI) works very differently than a traditional SFDI instrumentation that uses a sCMOS or CCD multi-pixel camera for detection. Recalling that images can be represented in terms of basis vectors and their respective coefficients, spSFDI samples the coefficients of the modulated light intensity projected by SFDI rather than its spatial domain representation. For SFDI, the advantages of the compressed sampling approach are, (1) the data acquisition rate could be improved by exploiting the redundancies of the sinusoidal modulation patterns, (2) the representation basis can be adjusted to represent a bandpass filter to remove undesirable frequency information, and (3) utilizes a single pixel detector that is cost effective and is far more sensitive than multi-pixel detector arrays especially in the IR range of light.

One of the main objectives of this thesis is to explore the potential of single pixel camera for quantification of the optical properties of a brain tissue simulating phantoms. Because, single pixel cameras are not yet commercial devices, we developed a unique, state-of-the-art single pixel imaging system for SFDI (spSFDI). A schematic of the setup is shown below along with the main components used to construct the system is shown below in Figure 3.1.



Single Pixel Camera Spatial Frequency Domain Imaging System Components

Component	Model Description
Source Illumination	660 nm Laser
SFDI Spatial Light Modulator	LightCrafter 4500
SPC Spatial Light Modulator	Vialux V-7001 DMD
SPC Detector	Hamamatsu C12703-01 APD
Data Acquisition Device	NI PCI-5122 Oscilloscope Card

Figure 3.1: Diagram and component list of single pixel spatial frequency domain imaging (spSFDI) instrument used to measure optical properties of brain tissue simulating phantom.

A laser shines light onto DMD I, which projects modulated light onto the turbid media. A convex lens is used to widen the modulated light's field of view to an area of 40 mm by 40 mm. Backscattered light from the turbid media is collimated onto DMD II in order to encode the scenery with the Bernoulli measurement matrices. From there, light reflecting from the ON state mirrors of DMD II is focused onto the active area of an avalanche photodiode (APD) via Lens Group II. An image of the spSF DI instrument constructed in the lab is shown in Figure 3.2 below.

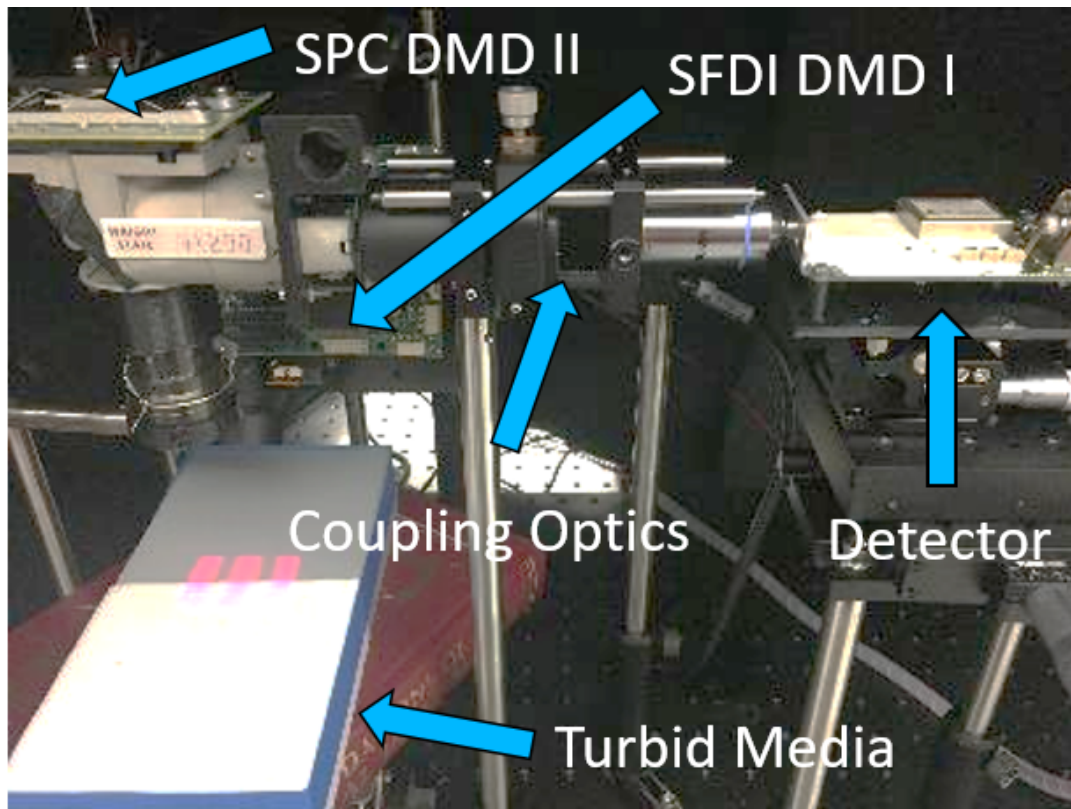


Figure 3.2: SPC SFDI prototype constructed in lab. The SPC DMD II reflects backscattering light from the Turbid Media the Coupling Optics, which focuses light onto the active area of the Detector.

The main difference between the spSF DI in this setup and the compressed single pixel SF DI setup mentioned in Chapter 2 is the use of a second DMD to generate and project the SF DI patterns instead using a fixed pattern generated by a film mask. Using a second DMD to project the spatially modulated light is highly convenient, because it allows the

SFDI projections to be changed with high speed and can deliver other patterns if needed. With the film mask method of producing the modulated light, the mask must be carefully shifted for each phase angle and exchanged for each spatial frequency, which is not viable for clinical SFDI.

However, using a second spatial light modulator (DMD) poses technical challenges related to the rapid movement of the micromirrors on the DMD chip. Because DMDs are only capable of projecting binary patterns, the SFDI patterns projected onto the turbid media are actually a collection of binary patterns. For this thesis, the SFDI patterns are composed of 8 binary planes that correspond to the `UINT8` format. The binary composition of an SFDI pattern is shown in Figure 3.3.

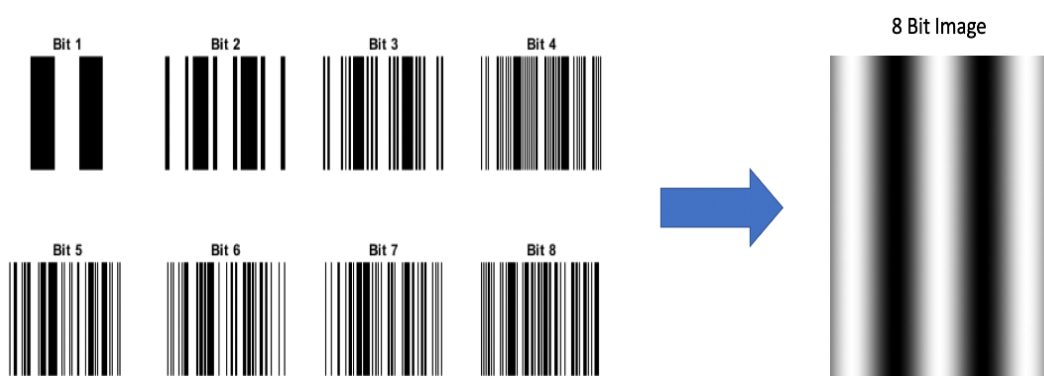


Figure 3.3: Binary composition of SFDI pattern. Bit 1 indicates the most significant bit.

The DMD rapidly projects the patterns, like the one shown in Figure 3.3, to create the illusion of a continuous sinusoidal wave projected along the horizontal axis from the perspective of a human's eye. This poses an issue for the single pixel camera if a single measurement is captured for each linear measurement in the measurement vector, g , since only one-bit plane will be sampled instead of all eight bits. One approach to avoid this issue is to collect many measurements for a single entry in g then average. The measurement vector collected for the first hundred measurements (averaged) is shown in Figure 3.4.

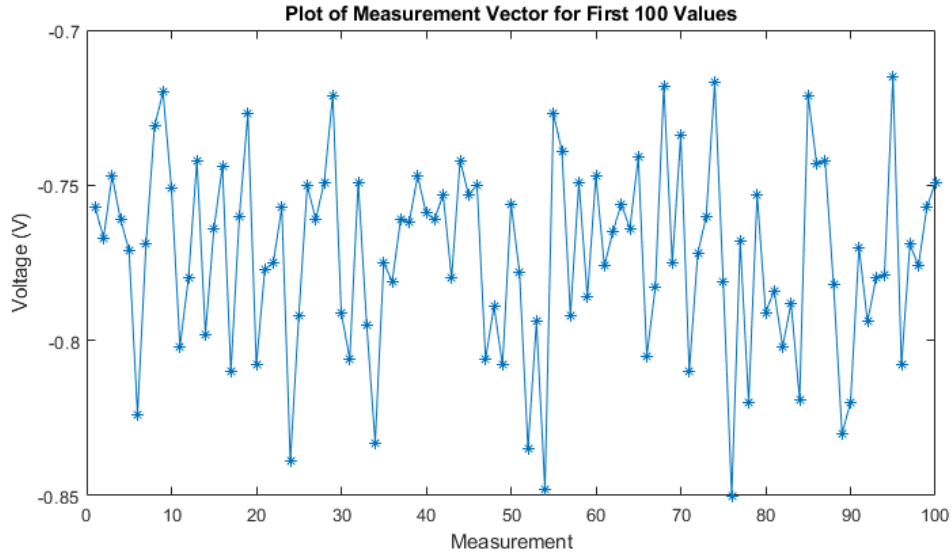


Figure 3.4: First 100 samples from measurement vector collected from spSF DI instrument. For each measurement, 1000 samples were recorded then averaged to account for the rapid movement of projection DMD.

Notice the measurements are in volts. The reason for this is because the avalanche photodiode emits a voltage signal that is proportional to the inner product of the K^{th} measurement vector. To measure the influence of undersampling on optical property contrast quantification accuracy, the measurement vector, g , is fully sampled meaning there is a measurement for each of the 4096 pixels in the projected SF DI scenery.

3.1.1 spSF DI Instrument Response Characterization with Brain Tissue Mimicking Phantoms

To characterize the response of the prototype spSF DI instrument developed, a brain tissue simulating phantom was imaged using both a spSF DI and a traditional multi-pixel camera based SF DI instrument in the lab. The multi-pixel based camera based SF DI setup is a well-known implementation called open-SF DI [1]. The open-SF DI setup in the lab is shown in Figure 3.5.

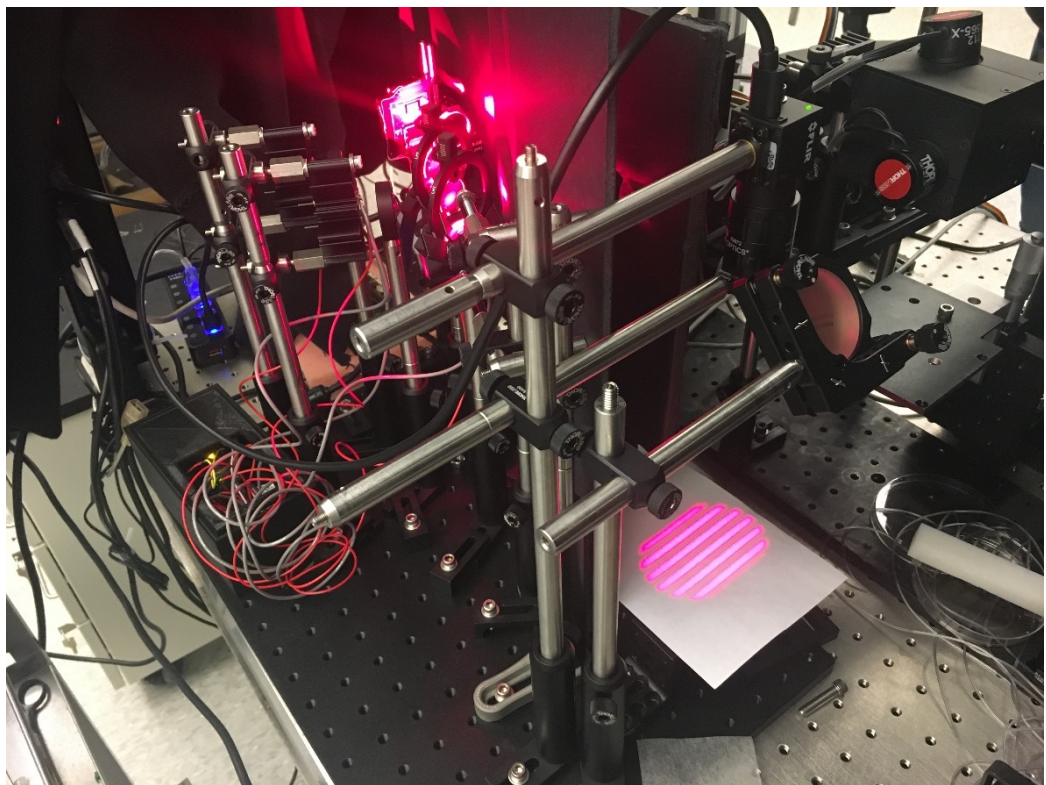


Figure 3.5: Image of open-SFDI system constructed in lab to compare against prototype SPC SFDI setup.

To compare the optical property quantification between the camera and single pixel based SFDI instruments, a brain tissue simulating phantoms with known optical absorption and scattering parameters were imaged with 660 nm light as the illumination source. An image of the phantom with spatially modulated light projected on the surface is presented in Figure 3.6.

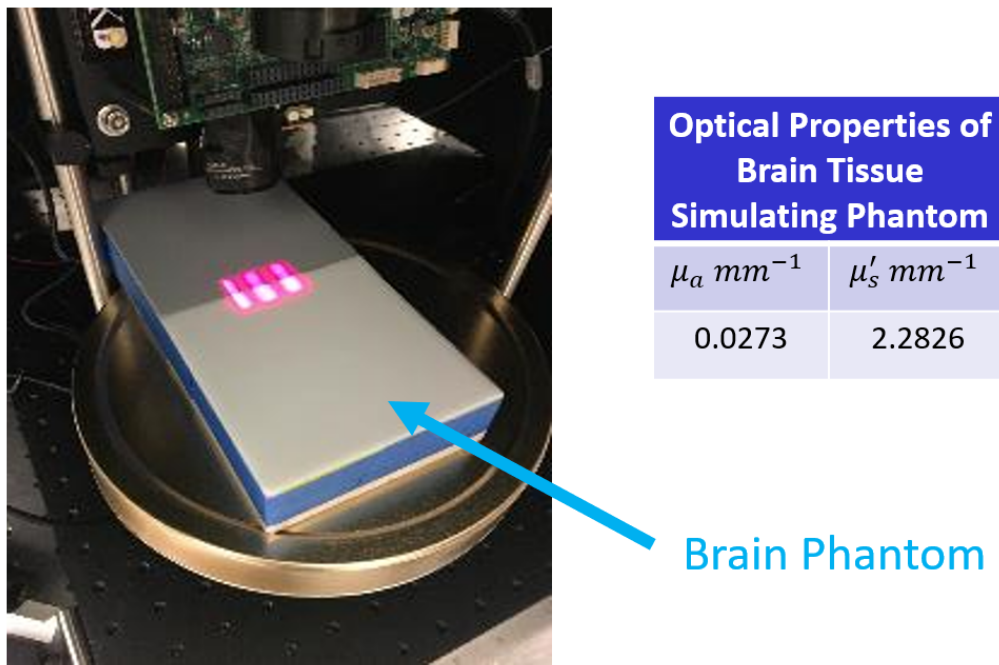


Figure 3.6: Optical property quantification of brain simulating phantom using camera and single pixel camera based spatial frequency domain instruments.

To avoid boundary related issues, 20x20 pixel regions of interest (ROI) were selected from the optical property maps for the determination of the quantification accuracy of the both methods by comparing to the expected values. Furthermore, the spSF DI instrument was 100% sampled for the ideal case and 50% sampled to compare the determine the influence of undersampling on optical property quantification accuracy. The results are shown below in Figure 3.7.

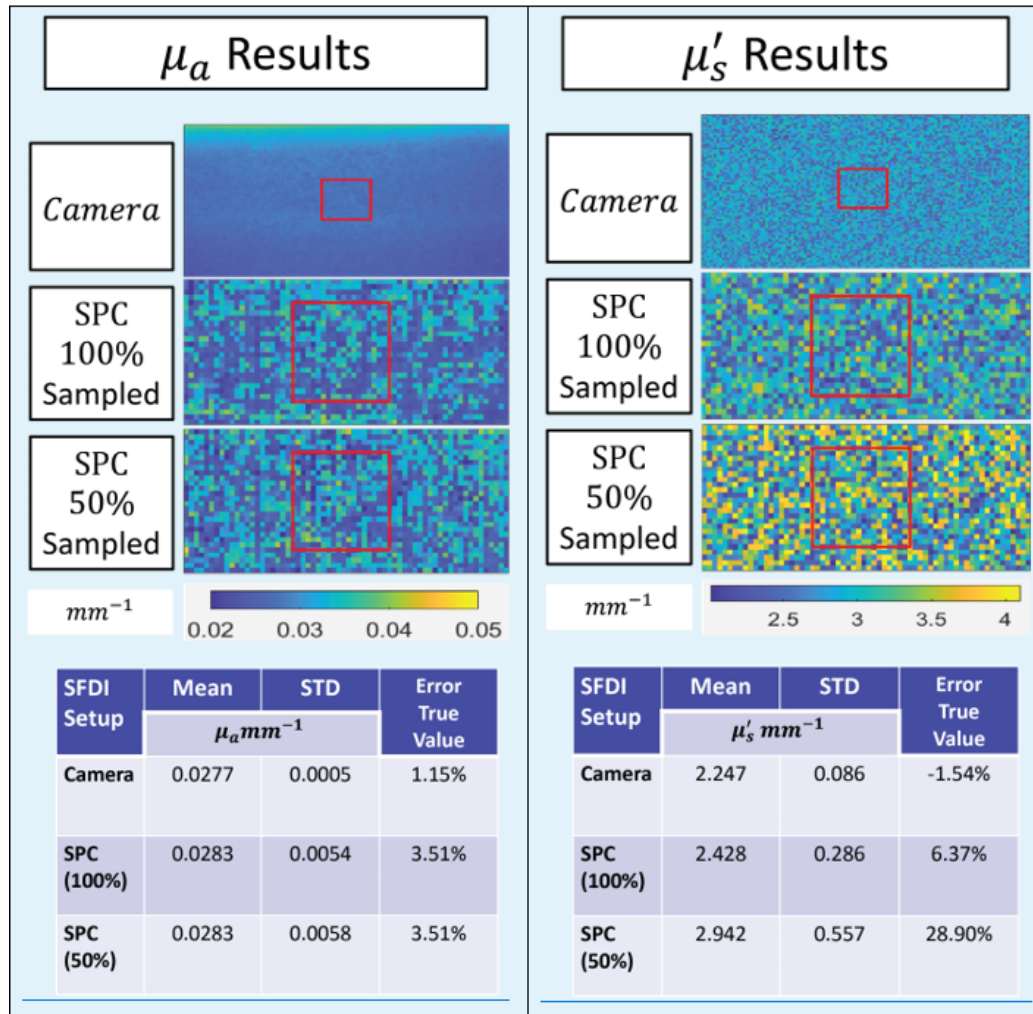


Figure 3.7: Optical property quantification of brain simulating phantom using camera and single pixel camera based spatial frequency domain instruments.

In general, the optical absorption quantification was more accurate for both instruments compared to optical scattering. The higher error in optical scattering quantification may be due to unoptimized spatial frequency selection. High spatial frequency is needed for higher sensitivity to scattering parameter. It is clear that the selected 0.1 mm^{-1} was not sufficiently high enough, and future experiments needs to be optimized such that at least one data acquisition higher than 0.1 mm^{-1} spatial frequency is expected to increase the accuracy in scattering parameter estimation. The camera-based system provided a high accuracy in absorption parameter quantification with a mean percent error of 1.2%, whereas spSFDI had a mean percent error of 3.5%. While the optical absorption quantification accuracy for both 100% and 50% sampling were the same in the spSFDI case, the variation (standard deviation) was higher for the 50% sampling case. The optical scattering parameter quantification accuracy for the camera-based system was high ($\sim 2\%$ error), but spSFDI had higher quantification accuracy error of $\sim 29\%$.

Conclusions and Future Works

4.1 Real-Time Single Pixel Imaging

Compressed sensing algorithms, typically used to reconstruct single pixel camera images, are iterative and computationally expensive, which has led to single pixel imaging systems not being capable of reconstructing images at video-like frame rates. An alternative approach is to train an artificially intelligent auto-encoder to translate the measurement coefficients into an image to eliminate the computational overhead from optimization. In recent work, a deep learning based autoencoder was used to reconstruct data from a single pixel camera to achieve video rate single pixel imaging [9]. A diagram of their convolutional neural network model is presented in Figure 4.1.

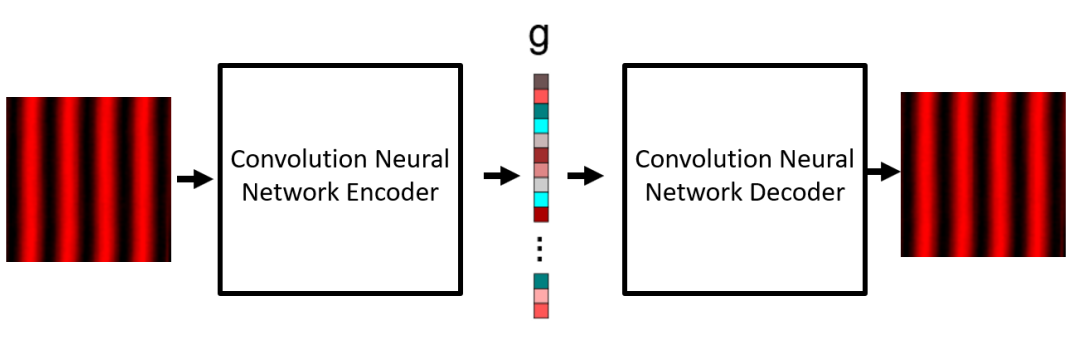


Figure 4.1: Convolutional neural network implemented to achieve single pixel imaging frame rates. The network encodes the input image with a set of learned Bernoulli measurement matrices. Following encoding, a decoding network transforms the latent space representation (or g) into an image.

An autoencoder is composed of three main parts; an encoding layer, latent space, and decoding layer. The encoding layer, in the case of single pixel imaging, is a set of basis vectors that encapsulates the information of the scenery being imaged into a vector of coefficients known as the latent space. The latent variables are input into the decoding layers, which are transformed into the expected image.

This approach to recovering the image places computational load during the training phase of the model, so image recovery is simply a set of matrix multiplication operations that are very efficient to compute. This is much quicker than trying to find the solution to a convex function through minimization. This approach to image recovery from the measurement vector is essential to realizing clinical SFDI. Otherwise, data acquisition would be too slow resulting in slow optical property map frame rates.

4.2 Real-Time SFDI Optical Property Map Extraction with Deep Learning

Optical property map extraction from reflectance data collected from SFDI requires optimization algorithms. Unfortunately, optimization algorithms tend to be slow, especially when the dimensionality of the problem is immense. In prior works, look up tables (LUT) were implemented to increase optical property map quantification rate [5]. While the LUT method is a simpler problem to optimize, it still lacks speed when data throughput is less than nominal.

The strategy of using deep learning to extract images from the measurement vector in single pixel imaging can be applied in spatial frequency domain imaging to acquire the optical property maps from reflectance image data. In previous works, fully connected deep learning neural networks were used to quantify optical property maps [19]. High resolution optical property maps of brain tissue simulating phantoms imaged in our lab are presented

in Figure 4.2.

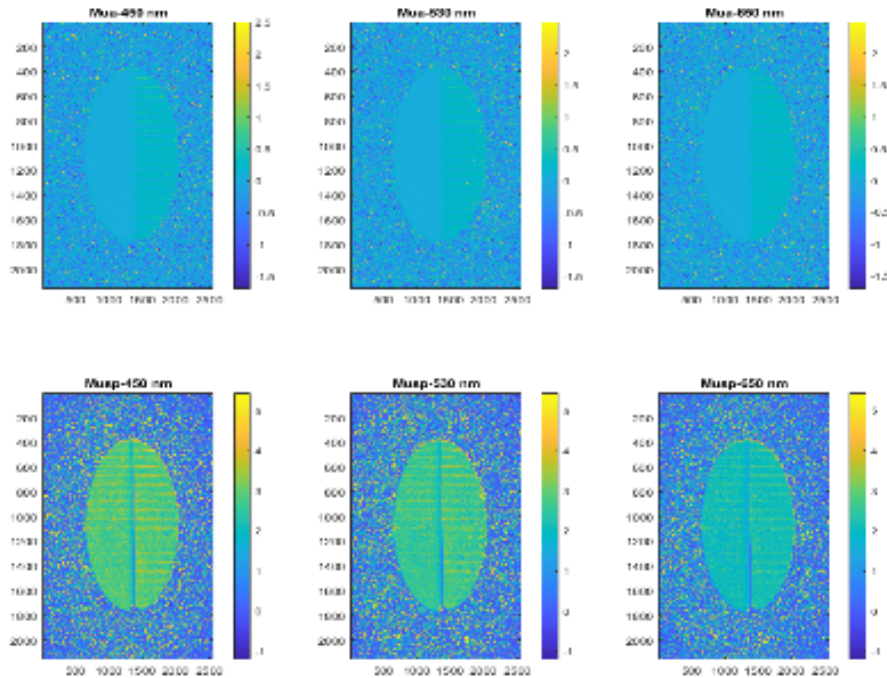


Figure 4.2: Optical property maps of brain tissue simulating phantoms imaged in our lab. The left and right center regions are liquid brain tissue simulating phantoms (noise outside perimeter from not imaging phantom).

Computation of these optical property maps is infeasible using traditional optimization methods that fit the modulation transfer function of the reflectance data approximated by the diffusion equation. In the case of SPC SFDI, high resolution imaging would not be feasible, but deep learning would eliminate the potential bottleneck of reconstructing optical property maps.

4.3 Improving Signal to Noise Ratio of Single Pixel Camera

As mentioned in Chapter 2, a DMD is composed of millions of bacteria sized mirrors that selectively block or reflect light to represent the ON and OFF states. However, the OFF state is does not perfectly block like and corrupts the measurement vector [12]. This phenomenon is demonstrated in Figure 4.3.

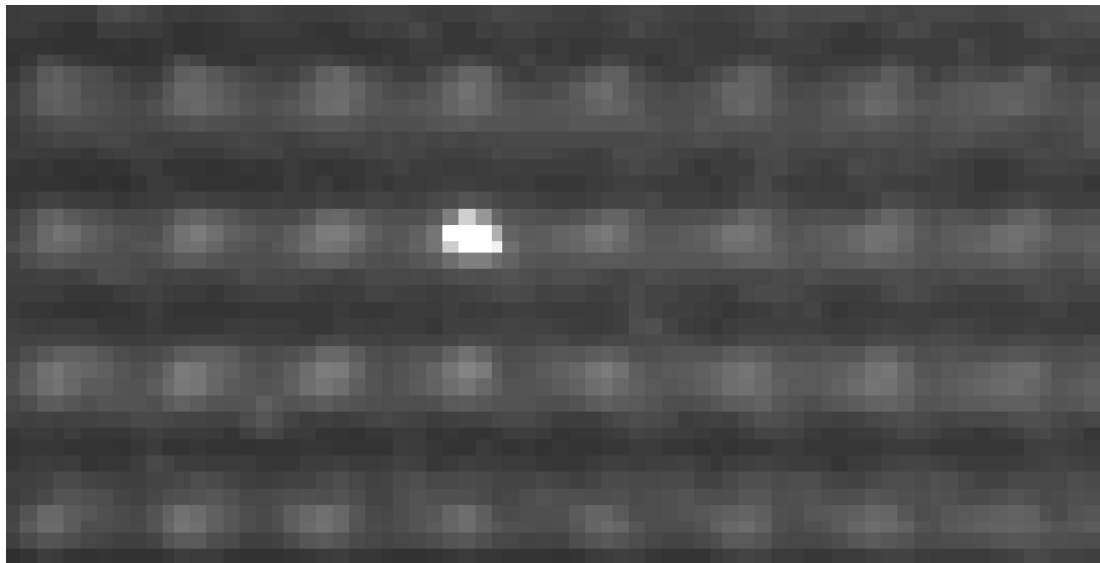


Figure 4.3: Image of single pixel camera DMD with only one mirror turned ON. The other faint light sources are OFF state mirrors that corrupt the measurement vector Image taken from “Calibration Models and System Development for Compressive Sensing with Micromirror Devices”[12].

In Figure 4.3, only one micromirror is in the ON state, while the other mirrors are in the OFF state. This phenomenon corrupts the measurement vector and degrades the overall image quality. A way to combat this issue is to measure the off-state gain from the light bleeding from the OFF-state mirrors. In prior work, an SPC that compensates for light bleeding was implemented [7, 14].

Bibliography

- [1] Matthew B. Applegate, Kavon Karrobi, Joseph P. Angelo, Wyatt M. Austin, Syeda M. Tabassum, Enagnon Aguénounon, Karissa Tilbury, Rolf B. Saager, Sylvain Gioux, and Darren M. Roblyer. OpenSFDI: an open-source guide for constructing a spatial frequency domain imaging system. *Journal of Biomedical Optics*, 25(01):1, 2020.
- [2] E J Candes and M B Wakin. An Introduction To Compressive Sampling. *IEEE Signal Processing Magazine*, 25(2):21–30, mar 2008.
- [3] Emmanuel Candès and Justin Romberg. 11-magic : Recovery of Sparse Signals via Convex Programming 1 Seven problems. Technical report, Stanford University, 2005.
- [4] Emmanuel J Candès, Yonina C Eldar, Deanna Needell, and Paige Randall. Compressed sensing with coherent and redundant dictionaries. *Applied and Computational Harmonic Analysis*, 31:59–73, 2011.
- [5] David J. Cuccia, Frederic Bevilacqua, Anthony J. Durkin, Frederick R. Ayers, and Bruce J. Tromberg. Quantitation and mapping of tissue optical properties using modulated imaging. *Journal of Biomedical Optics*, 14(2):024012, 2009.
- [6] David J Cuccia, Frederic Bevilacqua, Anthony J Durkin, and Bruce J Tromberg. Modulated imaging: quantitative analysis and tomography of turbid media in the spatial-

frequency domain Experiments performed on turbid phantoms demonstrate that spatially modulated illumination facilitates quantitative wide-field optical property mapping. Technical Report 11, 2005.

- [7] Krzysztof M. Czajkowski, Anna Pastuszczak, and Rafał Kotyński. Real-time single-pixel video imaging with Fourier domain regularization. *Optics Express*, 26(16):20009, 2018.
- [8] Marco F. Duarte, Mark A. Davenport, Dharmpal Takhar, Jason N. Laska, Ting Sun, Kevin F. Kelly, and Richard G. Baraniuk. Single-pixel imaging via compressive sampling. *IEEE Signal Processing Magazine*, 25(2):83–91, 2008.
- [9] Catherine F Higham, Roderick Murray-Smith, Miles J Padgett, and Matthew P Edgar. Deep learning for real-time single-pixel video OPEN. 8:2369, 2018.
- [10] Alexander J. Lin, Maya A. Koike, Kim N. Green, Jae G. Kim, Amaan Mazhar, Tyler B. Rice, Frank M. Laferla, and Bruce J. Tromberg. Spatial frequency domain imaging of intrinsic optical property contrast in a mouse model of alzheimer’s disease. *Annals of Biomedical Engineering*, 39(4):1349–1357, 2011.
- [11] ANita Faul (Microsoft Research) M.E. Tipping. Fast Marginal Likelihood Maximization for Sparse Bayesian Models. *Igarss 2014*, (1):1–5, 2002.
- [12] Rebecca L. Profeta. Calibration Models and System Development for Compressive Sensing with Micromirror Arrays, 2017.
- [13] Henry W Querfurth and Frank M Laferla. Alzheimer’s Disease. 9:329–344, 2010.
- [14] F. Soldevila, P. Clemente, E. Tajahuerce, N. Uribe-Patarroyo, P. Andrés, and J. Lancis. Computational imaging with a balanced detector. *Scientific Reports*, 6(June):1–10, 2016.

- [15] Texas Instruments. TI DLP ® LightCrafter™ 4500 Evaluation Module User’s Guide. (July), 2017.
- [16] C. Tipping. Bayesian Compressive Sensing Matlab Codes.
- [17] Mohammad Torabzadeh, Il-Yong Park, Randy A. Bartels, Anthony J. Durkin, and Bruce J. Tromberg. Compressed single pixel imaging in the spatial frequency domain. *Journal of Biomedical Optics*, 22(3), 2017.
- [18] Robert H. Wilson, Christian Crouzet, Mohammad Torabzadeh, and Afsheen Bazrafkan. High-speed spatial frequency domain imaging of rat cortex detects dynamic optical and physiological properties following cardiac arrest and resuscitation. *Neurophotonics*, 4(04):1, 2017.
- [19] Yanyu Zhao, Yue Deng, Feng Bao, Hannah Peterson, Raeef Istfan, and Darren Roblyer. Deep learning model for ultrafast multifrequency optical property extractions for spatial frequency domain imaging. *Optics Letters*, 43(22):5669, 2018.